NON-LTE CALCULATION OF RADIATION FROM SOLAR-TYPE FLARES ON ACCRETION DISKS

Harjeet Kumar

A thesis submitted in partial fulfillment of
the requirements for the degree of
Master of Science

Department of Physics

Central Michigan University
Mount Pleasant, Michigan
August, 2011

Accepted by the Faculty of the College of Graduate Studies,

Central Michigan University, in partial fulfillment of

the requirements for the master's degree

Thesis Committee:

Glen Williams, Ph.D.	Committee Chair
Christopher Tycner, Ph.D.	Faculty Member
Juan Ernesto Peralta, Ph.D.	Faculty Member
August 19, 2011	Date of Defense
Roger Coles, Ed.D.	Dean College of Graduate Studies
December 8, 2011	Approved by the College of Graduate Studies

ACKNOWLEDGEMENTS

I would like to thank my advisor Dr. Glen Williams. He helped at each and every step of my research and thesis. His suggestions were gladly accepted and very helpful. Also, thanks to Dr. Tycner and Dr. Peralta for being on my committee, and for their valuable comments. I am thankful to all my friends who help me during this research work. Central Michigan University for their support, and the Physics department for providing this opportunity, is thanked as well. Last but not least my parents, brother, sister and little Rohit who supported me at every turn, and Sheru.

ABSTRACT

NON-LTE CALCULATION OF RADIATION FROM SOLAR-TYPE FLARES ON ACCRETION DISKS

by Harjeet Kumar

Cataclysmic variables are binary star systems which have a white dwarf primary star, and a normal main sequence secondary star, with orbital period in the range 1-10 hours. Angular momentum loss from the binary drives the transfer of mass from the secondary star to the white dwarf. This mass forms a rotating accretion disk around the white dwarf. The spectra of cataclysmic variables show strong emission lines of hydrogen, helium, and other elements, coming primarily from the accretion disk. However, current models of accretion disks in these systems predict that they should be too thick to produce significant line emission.

Following along with the work of Jeewoo Park, we have considered the possibility that solar-type flares on the surface of the accretion disk are the source of the line emission. Park's models of solar-type flares on accretion disks are the starting point for our radiative transfer calculations of the line and continuous emission from these flares. We have modified an existing non-LTE radiative transfer computer program to allow for a non-plane parallel geometry with cylindrical symmetry. The mean intensity at each of 1500 points (30 radial steps and 50 depth steps) is found by integrating the radiative transfer equation along 72 individual rays. The mean intensities at 75 frequencies are used to calculate the level populations of a 30-level hydrogen atom, and a 27-level helium atom by the technique known as non-Local Thermodynamic Equilibrium. Using

these level populations, new mean intensities are calculated. This process is repeated for 30-40 iterations, until a sufficient level of convergence has been reached.

Once a sufficient level of convergence had been reached, we calculated the line and continuous emission from the flare models. These results were compared with observations of solar flares from the literature. We found that the line emission from the Park flare models was weaker than observed on the Sun. In addition, the Balmer decrement ( ) was larger than observed in solar flares. Possible explanations for this discrepancy were discussed.

TABLE OF CONTENTS

LIST OF FIGURES

FIGURE PAGE

LIST OF TABLES

TABLE PAGE

CHAPTER I

INTRODUCTION

1.1 Overview of Cataclysmic Variables

Most of the stars in our galaxy are not single stars. They are binary stars (i.e. a pair of stars orbiting each other). The binaries in which one of the stars is a white dwarf the other is a red dwarf, and matter is transferred from the red dwarf to the white dwarf, are known as cataclysmic variables (CVs). The focus of my research is dealing with Cataclysmic Variables.

The white dwarf in a CV is commonly known as a primary star. It has a mass comparable to one solar mass, and a size comparable to Earth, which makes it a very dense star. The red dwarf is known as companion, or secondary star in the CV. They generally have a mass and radius smaller than the Sun. It is small, but still much larger than a white dwarf.

Both stars orbit each other with short orbital periods, typically hours. They are so close that the gravity of the white dwarf distorts the less dense companion, and material starts flowing from the companion to the white dwarf. The potential energy , specified by vector **r,** can be written as the sum of the gravitational potentials of the two stars with masses M_1 (primary star) and M_2 (secondary star) located at $\mathbf{r_1}$ and $\mathbf{r_2}$, and a centrifugal potential.

(1.1)

With increases in , the critical equipotential surface has a “figure 8” appearance and the point at which they come in contact is known as inner Lagrangian point L_1. In cataclysmic variables the companion star fills its Roche lobe and gas from the outer layers of the red dwarf starts transferring towards the white dwarf via an accretion disk. An accretion disk is the buildup of material orbiting the white dwarf, which eventually falls onto the star.

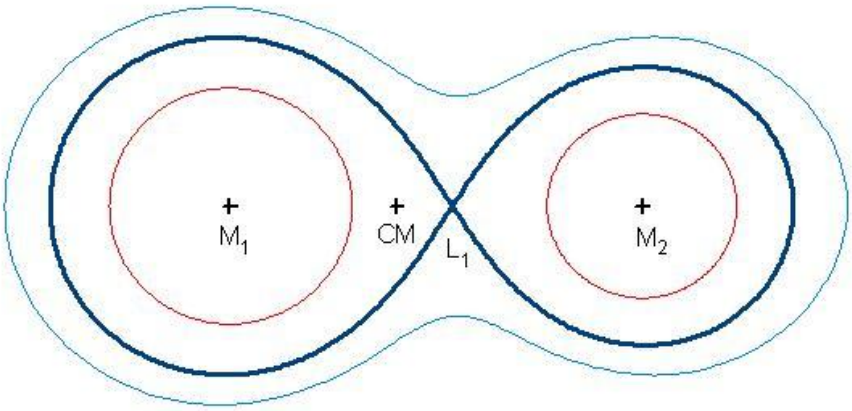

Figure 1.1. The Roche lobe geometry in a binary system.
Three equipotential surfaces are shown. The dark blue curve is the critical Roche surface.

Matter is transferred through the L_1 point as long as the secondary star remains in contact with its Roche lobe. This might happen for one of two reasons. First, the secondary star may be an evolved star which is expanding to fill its Roche lobe. Secondly, the orbit may be shrinking due to a loss of orbital angular momentum. This causes the Roche lobe to contract and come into contact with the secondary star. In this second scenario, orbital angular momentum loss from the system drives mass transfer from the secondary star to the white dwarf. In longer period systems (P>2.5 hours) the

angular momentum loss occurs due to magnetic braking, and in short period systems (P<2.5 hours) it occurs due to the emission of gravitational radiation from the binary.

Cataclysmic variables are categorized, in part, according to the magnetic field of the white dwarf. If the white dwarf's magnetic field is weak the accretion disk extends down to the surface of the white dwarf. This is the most common situation for CVs. In these systems, gas from the inner edge of the accretion disk settles onto the surface of the white dwarf via a hot 'boundary layer'. These systems are generally referred to as Dwarf Novae, Novae, or Nova-likes.

When the white dwarf's magnetic field strength is in the range (1-10 MGauss) an accretion disk forms, but does not extend to the surface of white dwarf. The inner edge of the accretion disk is 'truncated' at a point where the energy density of the gas equals the energy density of the magnetic field. Beyond this inner edge, the gas is carried along the magnetic field lines to the magnetic poles. Radiation from these poles illuminates the disk and the secondary star. As the white dwarf rotates with a period less than the orbital period, this illumination creates oscillations in the light curve. These systems are referred to as Intermediate Polars, or DQ Herculis Stars.

If the white dwarf's magnetic field is very strong (10-100 MGauss) there is no accretion disk. As the gas is partially ionized, and the charged particles cannot cross the magnetic field lines, the matter falls along the field lines directly at the magnetic poles of the white dwarf. Much of the radiation from these systems comes from 'accretion columns' above the magnetic poles. Also, in these systems, the white dwarf's very strong magnetic field causes the white dwarf to rotate synchronously with the binary orbit. These systems are referred to as Polars, or AM Herculis stars.

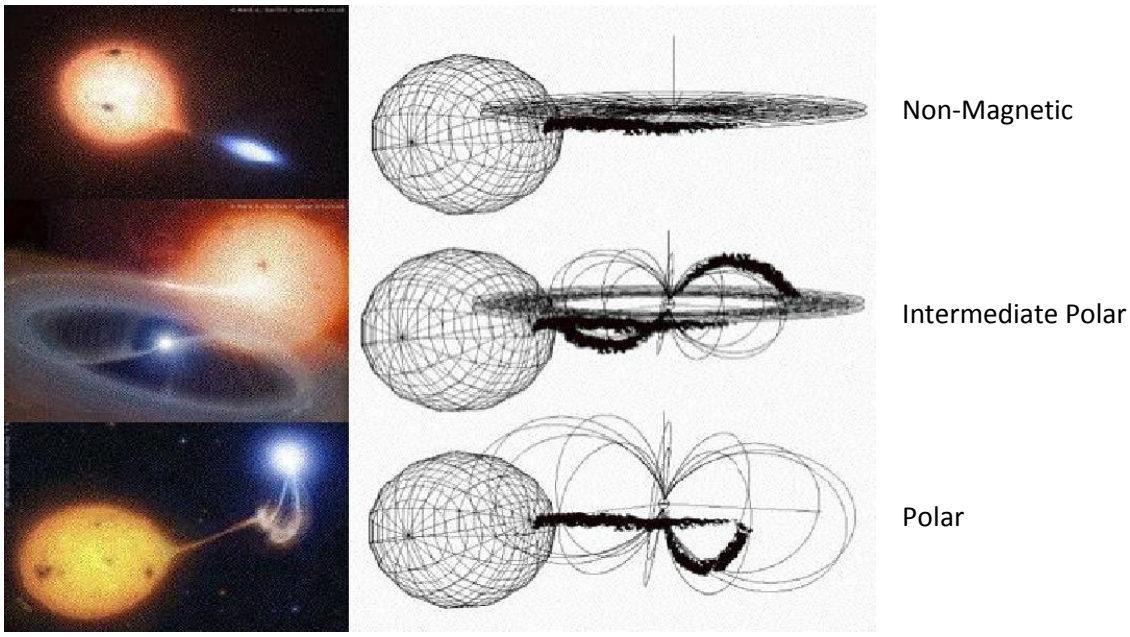

Figure 1.2. Three types of CVs based on white dwarf magnetic field strength. Used with permission of M. Cropper.

On certain occasions a cataclysmic variable can outburst. The outbursts of CVs can be divided in two subclasses known as Classical Novae and Dwarf Novae. The outbursts of Classical Novae are caused by rapid hydrogen fusion at the surface of the white dwarf. When the layer becomes deep enough, hydrogen fusion begins. After the outburst occurs, fresh hydrogen begins collecting at the surface again. Classical Novae are believed to reoccur approximately every 10,000 years.

The Dwarf Novae have outbursts which occur for a different reason, and have much less energy than classical novae outbursts. These are caused by a thermal instability in the accretion disk. When the density in the disk becomes too large, the viscosity increases, the gas moves rapidly inward through the disk. After the disk empties out following an outburst, gas starts collecting in the disk again. Dwarf Novae may reoccur as frequently as every month.

The light curves of Cataclysmic Variables show different types of variability. Typically seen in the light curves of CVs is a non-periodic, random variability called 'flickering'. Some flickering is known to occur at the 'hot spot' where the stream of gas from the inner Lagrangian point hits the outer edge of the accretion disk. Flickering may also occur at the inner edge of the accretion disk, where blobs of gas land on the surface of the white dwarf. Another possible source of flickering may be solar-type flares at the surface of the accretion disk.

Some systems also show quasi-periodic oscillations (QPOs) in the light curve. In QPOs variability does not occur on a preferred time scale and only lasts for a few cycles. They are believed to be due to temporary structures at the inner edge of disk. They have very low coherence.

A third type of variability seen in the light curves of some CVs is called Dwarf Nova Oscillations. These are only seen during the outburst of dwarf novae and have a shorter period than QPOs. These are believed to be due to gas accreted at the equator of the white dwarf. They have greater coherence than QPOs.

1.2 Spectra of CVs

All of the information we can obtain about a star comes from the electromagnetic radiation we receive from it. Today observations of CV may be made across the entire electromagnetic spectrum. In CVs the optical radiation comes from the accretion disk, the gas stream from the secondary star, the 'hot spot' where the gas stream hits the disk, and the primary and secondary stars. But the accretion disk is generally the most prominent source of optical radiation. The stars' spectra show absorption lines, whereas the lines from the disk generally have emission characteristics, with strong emission lines

of H, He I, He II, Ca II and Fe (Williams, 1983). Figure 1.3 shows the optical spectra of several CVs. The emission lines from the disk are quite often double peaked due to the Doppler shift of radiation from gas on opposite sides of the accretion disk, when the disk is seen at a moderate to high inclination angles. On one side the gas is approaching the observer, and on the other side it is receding. Gas orbiting near the white dwarf will have the highest velocity, and thus the largest Doppler shift. If the disk is viewed nearly face-on, the lines will appear single peaked.

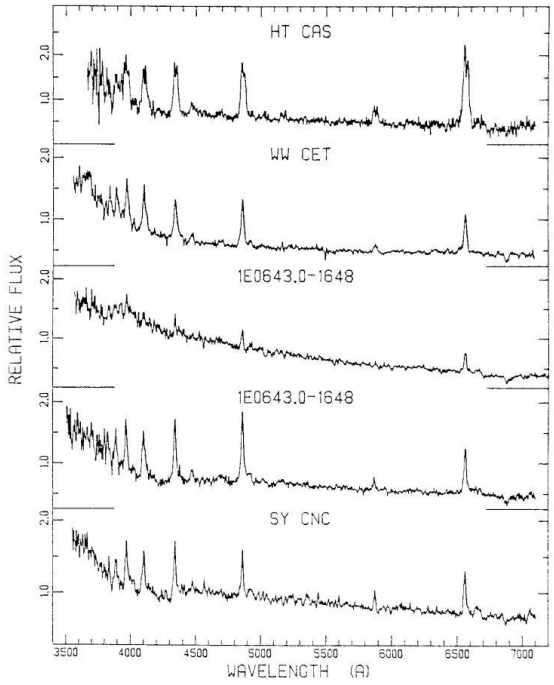

Figure 1.3 The Optical spectra of several CVs (Williams, 1983)

In accretion disks when the optical thickness in the continuum is less than one, the gas is considered as optically thin, but if the optical thickness for the line photon is significant, then an emission spectrum is produced. Accretion disk models of Williams, R. (1980, 1991), Tylenda (1981), Williams, R. & Ferguson (1982), and Williams, G. & Shipman (1988) are based on steady-state mass transfer through the disk. If the mass

transfer rate through the disk is then they have an optically thin region at the outer edge of the disk and it produces the line emissions. On the other hand, dwarf novae outburst models of Meyer & Meyer-Hofmeister (1981, 1982 and 1983), Cannizo, Shafter & Wheeler (1988), and Cannizzo (1993), assume low viscosity in quiescence. In these models the mass transfer rate through the disk is less than the mass transfer rate from the secondary, so gas builds up in the disk and it becomes optically thick. Thus, there are no emission lines.

In CV's there is a rough correlation between the accretion disk inclination angle, and the equivalent width of the emission lines. At higher inclination angles (i.e. disk seen more edge-on) the emission lines, generally, show a larger equivalent width. (The equivalent width of a line equals the wavelength-integrated intensity in the line above the continuum, divided by the intensity in the continuum.) For accretion disks which are optically thick in the continuum, the intensity in the continuum should decrease roughly as ; as the projected area of the disk decreases. The line emission may decreases as well, but not as fast, thus line equivalent width increases. The equivalent line widths are shown in figure 1.4 below for both low inclination and high inclination systems. This observation indicates that some of the line emission must come from above and below the accretion disk.

This line emission might be explained by chromospheric emissions (emission from the thin upper layer of the disk atmosphere). The mechanisms that can heat the chromosphere are viscous dissipation (Adam et al. 1988), magnetic loops arching out of the disk (Shakura and Sunyaev, 1973), irradiation by the boundary layer at the surface of the white dwarf, or the hot inner regions of the disk. Williams (1992) showed that

hydrogen line strengths may be increased by 25% as a result of a chromosphere produced by boundary layer radiation. This is not sufficient to explain the strong line emission from CVs. So there is some other source of radiation which emits emission lines. Williams and Maletesta (2001) proposed that solar-type flares on the surface of accretion disks might be the cause of these emission lines.

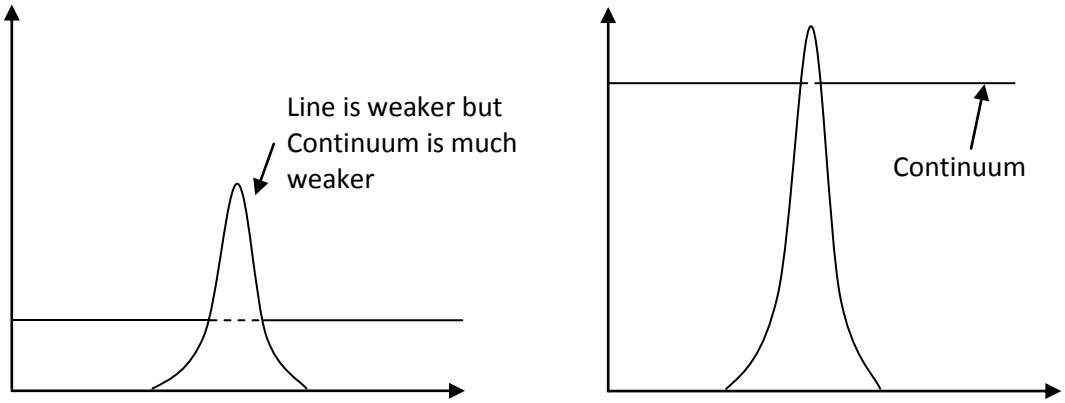

Figure 1.4. Variation of emission line equivalent width with inclination angle for CVs.

1.3 Motivation for This Work

There are three main reasons that have motivated our research. One of those was to determine, by using a CV system, if there is a possibility that solar-type flares on accretion disks can explain the emission line spectra of optically thick disks. Also, to investigate if the flares could explain the flickering commonly seen in CV light curves. Another reason is to calculate non-LTE radiative transfer in cylindrical space with azimuthal symmetry. We have performed radiative transfer calculations in non-plane-parallel atmosphere. To our knowledge we are the first to attempt this method using cylindrical geometry with azimuthal symmetry. Radiative transfer calculations have been performed in non-plane-parallel geometries (e.g. spherical), but not in a cylindrical space.

The last reason that motivated this research was to expand on the work done by Jeewoo Park. This would be done by calculating emission from his flare models.

CHAPTER II

ATOMIC DATA

2.1 Atomic Processes

To find level populations for hydrogen and helium we need to study the processes which take electrons out of the levels and processes which put electrons in to the level and their rates. The processes are explained below with a three level system.

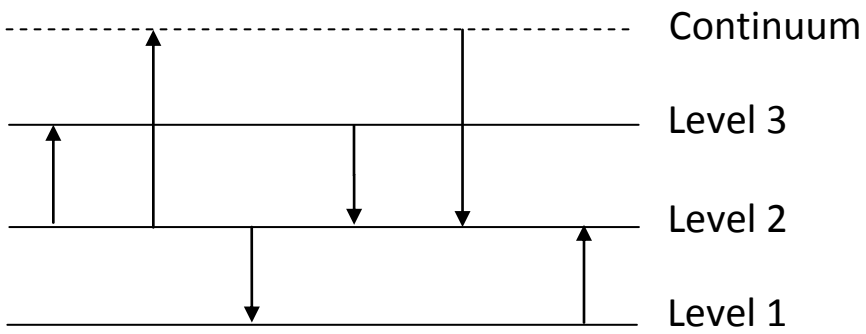

Figure 2.1. Illustration of transitions to and from level 2 in a hypothetical 3-level atom.

Processes which take electrons out of level 2 are:

1. Line Absorption or Collisional upward transition (Excitation)
2. Photoionization or Collisional ionization
3. Line Emission or Collisional downward transition (De-excitation)

Processes which put electrons in level 2 are:

1. Line Emission or Collision downward transition
2. Radiative Recombination or three-body recombination
3. Line Absorption or Collision Excitation

The rates at which these processes move electrons into or out of a level are given below.

2.1.1 Photoionization and Radiative Recombination

In photoionization, an electron absorbs a photon with energy greater than the ionization energy from the particular level in which the electron sits. The rate at which photoionizations remove electrons from level 2 is given by , where is the number density of atoms with the electron in level 2, and R is given by

(2.1)

Here is the mean intensity of radiation at the point, is the cross section for photon absorption, and is the frequency threshold for the ionization. The mean intensity at a point in the gas must be found by solving the radiative transfer equation. In general, the mean intensity depends on the conditions in the gas in the vicinity of the point. If however, the opacity of the gas is low, then radiation from distant points in the gas will contribute to the mean intensity.

Radiative recombination is the inverse process of photoionization. Here a free electron spontaneously recombines to some level of an ion, and emits a photon. The rate at which radiative recombination puts electrons into level 2 is . In this expression is the number density of ions, is the number density of free electrons, and is the radiative recombination rate coefficient for recombinations to level 2. The radiative recombination rate coefficient may be found from the principle of "Detailed Balancing". This says that in thermodynamic equilibrium, every atomic process is exactly balanced by its inverse process. In this context we could write

, where the asterisk represent the thermodynamic equilibrium values. In

thermodynamic equilibrium the relationship between the number densities for atoms in successive stages of ionization is given by the Saha equation

(2.2)

Here, and are the partition functions for the i and i+1 ionized stages, respectively. The ionization energy of stage i is . The number density of atoms with electrons in level j of atomic species i is given by the Boltzmann equation

(2.3)

Here, is the statistical weight of the j-th level, and is the excitation energy of this level. Combining these gives , or in our example, . Detailed balancing then gives

(2.4)

It is also worth noting that even though this relation was derived with the assumption of thermodynamic equilibrium, it applies generally; even when the gas is not in thermodynamic equilibrium.

2.1.2 Collisional Excitation and De-excitation

Collisional Excitation is the process in which an atom has an electron in a lower state (say, level 1), and a free electron collides with the atom, causing the electron to move to an excited state. The collisional excitation rate from level 1 to level 2 is given by

, where is the collisional excitation coefficient, and is defined by the following integral over collision velocity

(2.5)

here is known as cross section for collisional excitation, is the as Maxwell-Boltzmann velocity distribution, and is the threshold velocity. The collisional excitation coefficient is actually found from the collision strength ( ) whose values are tabulated as a function of temperature. The collisional excitation rate coefficient may be found from the collision strength with the relation

(2.6)

Collisional De-excitation is the inverse process of collision excitation. The rate of collisional de-excitation may be found from the principle of Detailed Balancing. In this case we have . As these are bound-bound transitions, only the Boltzmann equation applies. Thus, we have

(2.7)

2.1.3 Collisional Ionization and Three-Body Recombination

Collisional ionization is similar to collisional excitation, except that the upper level is the continuum. In this process an atom in ionization stage i collide with a free electron. After the ionization, the atom is in ionization stage i+1, and there are two free electrons. The rate of collisional ionization from level 2 in our example would be . As

with collisional excitation, the collisional ionization rate coefficient is found from the collision strength ( ) using equation 2.6. Here the upper level excitation energy is replaced with the ionization energy ( ), and the excitation of the lower level is .

The inverse process is called Three-Body Recombination, because it involves two free electrons and an ion. The rate of three-body recombination to level 2 is given by, . The three-body recombination rate coefficient is again found from the principle of Detailed Balancing. As a change in ionization state is involved, we have a formula similar to equation 2.4.

(2.8)

2.1.4 Radiative Bound-Bound Transitions

An electron in an excited state may spontaneously return to a lower state by emitting a photon. This transition may also be induced by a passing photon in a Stimulated Emission. The rate of downward radiative transitions from level 2 would be , where is the Einstein coefficient for the downward radiative transition. The Einstein A coefficients may be found in the literature, or they may be found from the Oscillator Strengths (f), which are also tabulated for each transition. The conversion is

(2.9)

The net rate of radiative absorption from level 1 to level 2 is given by . Here, is the Einstein coefficient for absorption, and is the Einstein

coefficient for stimulated emission, and is the mean intensity of line radiation. Detailed Balancing would give, in thermodynamic equilibrium

(2.10)

where the term in parenthesis is the correction for stimulated emission. Using the Boltzmann equation we may find .

Generally, the rates of radiatively permitted transitions are much larger than other atomic processes. In thermodynamic equilibrium, any photon emitted in a downward transition is immediately absorbed by a neighboring atom. Thus the rates of upward and downward radiative transitions balance exactly. If, on the other hand, some photons may escape from the gas, the gas will not be in thermodynamic equilibrium. In these cases, the net rate of downward radiative transitions (downward minus upward) is given by

(2.11)

where , is the probability of the photon's escape from the gas. Equation 2.11 is known as the "Net Radiative Bracket". Deep inside the atmosphere (or accretion disk) the probability of escape goes to zero, and so does the net rate of downward transitions.

2.2 Finding Collision Strengths

2.2.1 Atomic Data for Hydrogen

When working with hydrogen radiative rates (A-values or f-values), the data were taken from multiple sources. For n to n' transitions, Weise, Smith, and Glennon (1966) was used. When working with nl to n'l' transitions, data came from two sources: Capriotti and Green (1964), as well as Rush and Chandler (1957). Photoionization cross

sections were taken from Burgess (1964) for nl substates, and from Seaton (1959) for states with n greater than or equal to 6. Collisional excitation and ionization rates from state n to n' were taken from Johnson (1972). In earlier work (Williams and Shipman, 1988), rates for collisional transitions between states with the same principle quantum number (nl to nl') were taken from Brocklehurst (1971). Collisional transition rates of the form nl to n'l' were largely unknown in earlier work, so approximations were used.

2.2.2 Atomic Data for Helium

When working with helium radiative rates (A-values or f-values), the data were taken from C.E. Theodosiou (1987). Photoionization cross sections were obtained from the Opacity Project of the Ohio State University. The data are complete except for the 4^1F, 5^1F, 4^3F, and 5^3F levels. These photoionization cross sections were estimated by extrapolation. Previously, collisional excitation rates for 49 bound-bound transitions were taken from Berrington and Kingston (1987). Collisional excitation rates for other radiatively permitted transitions were calculated by Vriens and Smeets (1980). All other bound-bound rates were assumed to be zero. Rates for collisional ionization were calculated from the formulas of Vriens and Smeets (1980).

While most of the atomic data for hydrogen and helium are well known, and reliable, this was not the case for collisional transition rates (or collision strengths). Tables of collision strengths were incomplete, and mostly contained only approximate values. One of the main goals of this project was to search the literature for the most complete, up-to-date values for collision strengths. Our search led us to two sources: Chianti and CMFGEN.

2.2.3 Chianti

Chianti is self-described as an "Atomic Database for Spectroscopic Diagnostics of Astrophysical Plasmas". It consists of critically evaluated, up-to-date atomic data, in a database form. The data can be extracted using Interactive Data Language (IDL) programs. The Chianti package (software and data files) is freely available at www.chiantidatabase.org. The Chianti team members consists of Dr. Ken Dere (Naval Research Laboratory), Dr. Helen Mason (University of Cambridge), Prof. Brunella Monsignori-Fossi (Arcetri Astrophysical Observatory in Florence, Italy), Dr. Enrico Landi and Dr. Peter Young.

We used the latest version of the Chianti database; Chianti 6. It is distributed in two ways, within SolarSoft, a programming and data analysis environment, and as a stand-alone package. We used the Chianti stand-alone version for extracting collision strengths from the database.

We needed to collect the up-to-date tables of collision strengths at different temperatures for hydrogen and helium I. First of all, we noticed that the Chianti levels were not arranged according to our levels for both hydrogen and helium. Appendix C lists the hydrogen and helium I levels used in this work, along with our level designations, and those of Chianti. Using the Chianti level numbers, we wrote script files for use in the IDL program, so that we could extract the values of collision strength from the database. For hydrogen we got the values of collision strength for transitions from the levels 1 S, 2 S, and 2 P, to the other hydrogen levels. In the case of helium, we got the values of collision strength for transitions only from our level 1-^{1}S to other levels.

Collision strengths were extracted at 9 values of temperature ranging from 5012K to 251190K , and logarithmically spaced such that $\Delta \log T = 0.1$.

2.2.4 CMFGEN

CMFGEN is a Radiative transfer code designed to solve the radiative transfer and statistical equilibrium equations in spherical geometry. CMFGEN is freely available at http://kookaburra.phyast.pitt.edu/hillier/web/CMFGEN.htm. It is used in the modeling of O stars, Wolf-Rayet stars, Luminous Blue Variables and B supergiants (Hillier and Lanz 2001). Direct tables of collision strengths were available for hydrogen and helium at different temperatures. They are given at nine temperatures from 2,000K to 1,000,000K, and many values are constant above 50,000K. Again, we must convert our level number to those used by CMFGEN. The CMFGEN level numbers are compared to our numbers in Appendix C. For hydrogen we got most of the values of collision strength for different transitions. We got the values for transitions from our levels 1s, 2s, 2p, 3s, 3p, 3d, 4s, 4p, 4d, 4f, 5s, 6, 7, 8, 9, 10, 11, 12, 13, 14, 15, 16, 17, 18, 19 to different levels. In CMFGEN the values of collision strengths for transition from level 2p to level 13 looked as they were significantly larger than the values for similar transitions, so we interpolation to get those values in our table. For helium not all the values of collision strengths are available in CMFGEN, but we got most of them from it. We got the values for transitions from our levels 1-^{1}S, 2-^{1}S, 2-^{1}P, 3-^{1}S, 3-^{1}P, 3-^{1}D, 4-^{1}S, 4-^{1}P, 4-^{1}D, 4-^{1}F, 2-^{3}S, 2-^{3}P, 3-^{3}S, 3-^{3}P, 3-^{3}D, 4-^{3}S, 4-^{3}P, 4-^{3}D to different levels. Then the values are stored in to two separate files for Hydrogen and Helium. We used a Fortran77 program to combine the values from CHIANTI and CMFGEN into two separate files for Hydrogen and Helium according to our levels for different temperatures.

2.2.5 Filling In Missing Transitions

In CMFGEN the levels for hydrogen are broken in to L- substates up to n=4, and the data for n=5 L-substates was missing, so we used the formulas from M. Brocklehurst (1971) and L.C Johnson (1972) to fill these values in hydrogen table. Still some values for collision strengths were missing. We stored these values as zero in the data file.

There are some missing values of collision strengths in the helium table, as well. Unfortunately, we did not get any source to fill those values, so we set those values equal to zero in our data file for helium.

2.2.6 Collisional Ionization

All values of collision strength for the collisional ionization for both hydrogen and helium came from CMFGEN. For Helium, some of the values were missing, so these were estimated by extrapolation.

2.3 Using Collision Strengths in Our Program

As our radiative transfer program needs to evaluate the collision strengths at arbitrary temperatures, we decided to store the collision strength data as polynomial fits in temperature. For each transition, we used a Fortran program to do a 5th order, least-squares fit to the tabulated values. We chose to do the fit in terms of the logarithms of both collision strength and temperature. As such our fitting function was

$$\log \Omega = a_0 + a_1 (\log T) + a_2 (\log T)^2 + a_3 (\log T)^3 + a_4 (\log T)^4 + a_5 (\log T)^5. \qquad (2.12)$$

The coefficients of the fit were stored in two direct-access files, and were read into our radiative transfer program when the program began.

CHAPTER III

SOLAR FLARES

3.1 General Theory

The magnetic field under the photosphere of our Sun is very strong. The magnetic field lines extend toward the corona from the photosphere, and enter back in to the photosphere along loops. The loop has a positive footpoint from where magnetic field emerges out of the photosphere, and a negative footpoint where it returns into the photosphere. There is movement in the footpoints due to turbulent plasma motion under the photosphere. This photospheric disturbance transfers magnetic energy to the coronal magnetic field (Hughes, et.al. 2003). According to Romanova (1998), the turbulant motion in the photosphere of the sun can cause a twisting of the magnetic field lines, and eventually oppositely directed field lines may come in contact. When this happens, a magnetic reconnection event occurs, as the oppositely directed field lines cancel each other. The magnetic energy stored in these field lines is released, and electrons and ions are accelerated away from the site of the reconnection event. Because of their low mass, electrons are accelerated to especially high velocities. As their velocity increases, their cross section for collisions with other particles decreases, and so they can accelerate to even higher velocities. These "runaway" electrons also penetrate farther down in the photosphere than do ions, so only the heating by electrons is considered in solar flare models. The electrons, moving downward along the magnetic field lines, release their energy at some particular depth in the photosphere, creating an explosion at this depth.

The gas below this depth is compressed downward, and the gas above this depth is pushed explosively upward (Williams and Maletesta, 2001).

Many researchers have modeled solar flares on the surface of the sun. These models may differ in terms of their treatment of the electron heating, hydrodynamics, or radiative transfer effects. Often the hydrodynamics is one-dimensional, because the superathermal electrons and the plasma are constrained to move along the magnetic field lines. Many of the models today combine the hydrodynamics calculation with a non-LTE radiative transfer calculation. For example, Abbet and Hawley (1999) used a one-dimensional, adaptive grid on which to solve the hydrodynamics equations. They also used the non-LTE radiative hydrodynamic code of Carlsson and Stein (1997) to solve the plane-parallel equations of radiative transfer.

Williams and Maletesta (2001) used a two-dimensional, fixed grid, hydrodynamic code to model the flares on the accretion disks of CVs. Their simulations vary the energy flux, and duration, of the beam of superathermal electron. The plane-parallel, non-LTE radiative transfer program was then used to calculate the emission in the continuum, as well as the Balmer line emission.

3.2 Jeewoo's Models

My classmate Jeewoo Park did his research project with Dr. Williams to model solar-type flares on the accretion disks of CVs. They made several models to understand the atmosphere of the flare during the heating phase. In their models 3D hydrodynamic equations are solved by the method of Smoothed Particle Hydrodynamics (SPH). They also considered the effects of background magnetic field in their research. In their models they assume the pre-flare accretion disk is isothermal vertically, with temperature

3500 K. The flare is assumed to occur in the disk at a distance r from the white dwarf. The model space is rectangular, with the vertical direction perpendicular to the disk. The vertical height of the model space was several times larger than the horizontal width. The bottom of the model space was above the disk midplane, and set so that essentially none of the non-thermal electrons could reach this depth. A series of models were calculated varying (1) the maximum energy flux of the non-thermal electron beam, (2) the duration of beam heating, (3) the distribution of the non-thermal electron beam with radial distance from the central vertical axis of the model, and (4) the strength of the background magnetic field. The maximum energy flux of the non-thermal electron beam was varied from to . The magnetic field strength varied from 50 Gauss to 150 Gauss. These values were chosen because they are typical of solar flares.

Smoothed Particle Hydrodynamics (Lucy 1977, Gingold and Monaghan 1977, Monaghan 1992) is a numerical technique which divides a fluid into N discreet particles, and follows the time evolution of these particles. The hydrodynamic equations for the density, velocity, and specific internal energy of these moving particles are (neglecting magnetic fields)

— (3.1)

These derivatives are called “material derivatives” because they refer to the time evolution of the moving particles.

In SPH, the properties of the fluid at any point may be found by forming a weighted average of the properties of the particles within a certain distance from that point. The weighting function is called the “kernel”, and it is a function that has its greatest value at the center, and goes to zero at some finite distance. The average of some function may be written as an integral over volume as

(3.2)

here, W is the weighting kernel, and h is a scale factor. In SPH this integral is turned into a summation over some number of particles. Equation 3.2 then becomes

— (3.3)

where the first term inside the summation equals the volume taken up by particle b. The gradient of the function is

— (3.4)

By writing the hydrodynamic equations (3.1) in this form, we can find the time evolution of the properties of each particle.

CHAPTER IV

RADIATIVE TRANSFER

4.1 The Transfer Equation

Solving the equation of radiation transfer in the vicinity of a solar-type flare is a significant part of this thesis, and as such we will briefly outline its derivation. In section 4.2 we will discuss a powerful technique used to solve this equation in plane-parallel atmospheres. Finally, in section 4.3 we shall describe how this equation is solved in a non-plane parallel situation, such as a flare on an accretion disk.

The following diagram shows a ray travelling through a slab of gas with specific intensity and having units of (ergs cm^{-2} s^{-1} Hz^{-1} $ster^{-1}$).

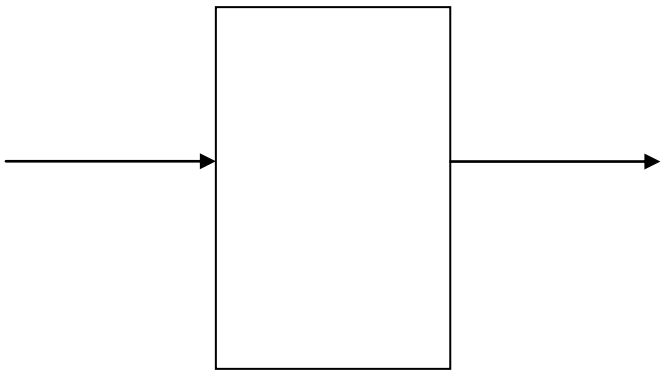

Figure 4.1. Radiation traveling along a ray through a slab of gas.

The intensity leaving the slab is , which may be written, , where is the change in specific intensity in the slab. In the slab radiation may either be removed from the beam, or added to the beam. The change in specific intensity of the beam is written as . The first term represents radiation removed from

the beam. This is equal to the product of the specific intensity of the beam, the "absorption coefficient" (also known as the "opacity"), and the slab thickness. The second term is the intensity added to the beam in the slab. Here, j, is the "emission coefficient". If we divide both sides of this equation by the slab thickness we obtain the equation

— (4.1)

the subscript, , indicates that the equation refers to one specific frequency. We can now divide both sides of the equation by the absorption coefficient, , to obtain

—— — (4.2)

We now define the dimensionless "optical depth" as, , and the "source function" as —. With these definitions we obtain the equation of radiative transfer in terms of the optical depth as

— (4.3)

The general solution of this first order differential equation is

(4.4)

The first term is the attenuation of the radiation entering the slab, and the second term is the intensity put into the beam in the slab. This is illustrated in figure 4.2.

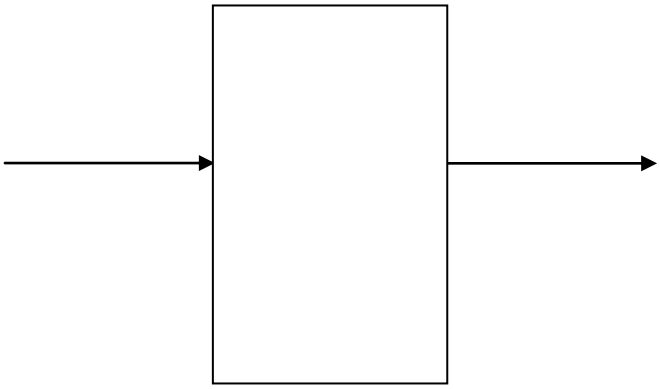

Figure 4.2. Radiation traveling through a slab of optical depth .

The Source function is equal to Planck function in Thermodynamic equilibrium, and in Local Thermodynamic equilibrium (LTE), . This assumes that the radiation is emitted and absorbed locally. If some of the radiation at a point comes from farther away, and if the radiation might be scattered locally, then the Source function is written as

(4.5)

where is scattering ratio, and is given by,

(4.6)

When , then ; and when , then . The mean intensity of radiation at a point, , is defined as

, (4.7)

where = element of solid angle.

4.2 The Plane Parallel Approximation

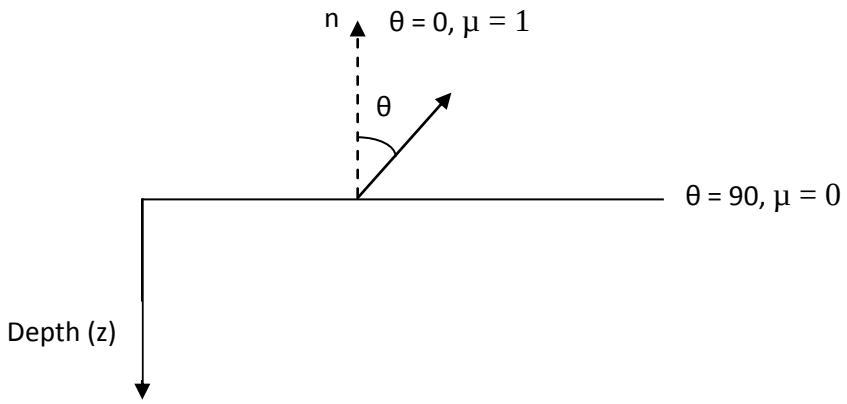

Figure 4.3. Geometry of a plane parallel atmosphere.

In the plane parallel atmosphere, temperature T(z), density ρ(z), optical depth τ(z), mean intensity (z), and the level populations of an atom $N_{i,j}$(z) are function of vertical depth only. The atmosphere is divided into plane parallel layers, and the angle made by the ray with the normal (n) to the layers is θ (μ = cosθ). The depth z is perpendicular to the plane-parallel atmospheric layers. If is the path length along the ray, then , and the vertical optical depth increment is . The transfer equation along the ray is then given by

— (4.8)

where is a function of depth, frequency and angle.

4.2.1 The Feautier method

A very powerful method for solving the transfer equation in a plane parallel atmosphere was developed by Feautrier (1964). While this method is not used in this thesis, we shall summarize it briefly so that a comparison may be made between solving

the transfer equation in a plane parallel geometry, and the non-plane parallel geometry used here. In the Feautrier method the transfer equation is expressed as a second order differential equation, changed to a difference equation, and solved numerically at some specific number of depths (typically). Boundary conditions must be applied at the top and bottom of the atmosphere before the solution may be found.

We can divide the specific intensity at a point into two components; one component moving into the atmosphere , and other component moving out of the atmosphere . The equation of transfer for each component is written as

— $-1 \leq \mu \leq 0,$ (4.9)

— $0 \leq \mu \leq 1.$ (4.10)

We now define two new variables as follows,

– , (4.11)

and – . (4.12)

Here is a mean-intensity–like variable, and is flux-like variable. By adding equations 4.9 and 4.10, and using equations 4.11 and 4.12, we get

——— , (4.13)

and by subtracting 4.9 and 4.10, and using 4.11 and 4.12, we get

——— . (4.14)

Using the expression for from equation 4.14 in equation 4.13, we get the second order differential equation

———— , (4.15)

where

Equation 4.15 is now converted into a difference equation using the standard representation of the second derivative in terms of finite differences. Boundary conditions must be applied at the top and bottom of the atmosphere, and also converted into difference equations. We now have a system of simultaneous equations where the value of u at some depth i, is only dependent on the values of u at depth i-1 and i+1. Even though we have a system of N ( ) simultaneous equations, these equations are tri-diagonal, and so the solution by Gaussian Elimination (or similar method) is very fast and efficient. This procedure must be applied at each continuum frequency.

4.3 Radiative Transfer in a Non-Plane Parallel Geometry

The flare geometry that we will use for our radiative transfer calculations is similar to that used by Park (2010) for his flare models. His model space was a rectangular cube, which we converted to a cylindrically symmetric model space. The central axis of the cylinder was vertical, and the model had an azimuthal symmetry around the central axis. In this geometry the temperature T_f (z, r), density ρ_f (z, r), optical depth τ_f (z, r), mean intensity (z, r), and level populations of an atoms $N_{i,j}$ (z, r), are functions of both vertical depth, and radial distance from the central axis. In the k outside the cylindrical region of our flare, each of these quantities was only a function of vertical depth (i.e. T_a (z), ρ_a (z), etc.). Figure 4.4 shows this geometry.

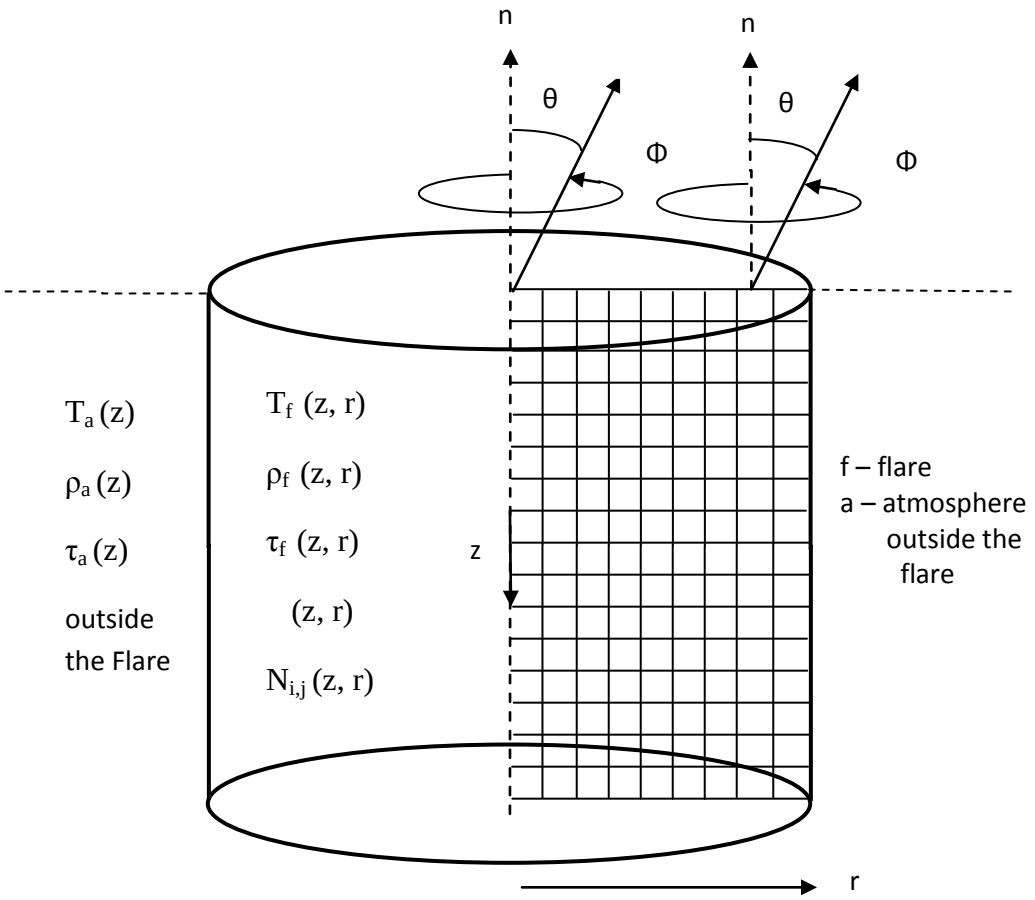

Figure 4.4. The cylindrical geometry of our flare models.

The specific intensity is a function of the angle (θ) from the normal, azimuth angle (Φ), and radial distance from the central axis of the cylinder. We divide the vertical height into 50 depth steps (along z), and radial distance into 30 radial steps (along r) from the central axis. In our flare model space we have 1500 points. Solving for the radiation field in this model space means finding the mean intensity of radiation, J, at each of these 1500 points.

Our method of finding the mean intensity of radiation at each point involved solving the transfer equation along many individual rays which all converge on the point in

question. The space around each point was divided into 6 angles from the normal ( ), and 12 azimuthal angles ( ). These angles were chosen to be abscissas of a 6-point Gaussian integration, running from 0 to in ; and 0 to , and to in (Abramowitz and Stegun, 1970). Along these 72 directions we imagine two rays approaching the point from opposite directions. One ray approaches the point from above (I_{in}), and the other approaches the point from below (I_{out}) as shown in Fig 4.6. When viewed in this way, the rays cover a solid angle of sterradians. The other sterradians are identical by symmetry. These 72 angles are illustrated in Figure 4.5.

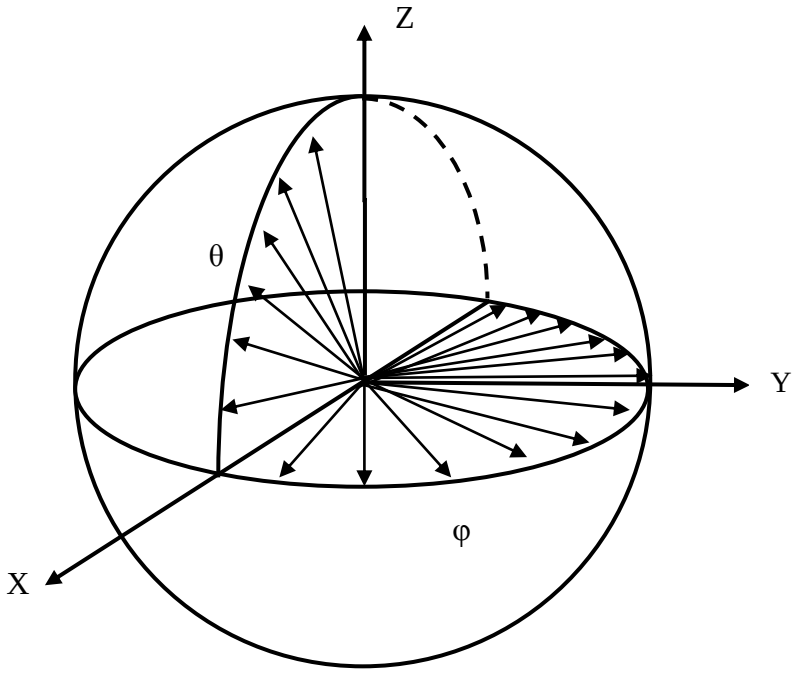

Figure 4.5 Illustration of the altitudinal and azimuthal rays used in the transfer calculation.

The specific intensity approaching the point along each ray is now calculated using equation 4.4.

(4.16)

Along each ray the optical depth is chosen to increase away from the point. The second term gives the radiation put into the beam along the ray. The first term is the attenuation of radiation input at the end of the ray. For rays coming from above the point, the intensity ( ) would represent any possible illumination at the top of the accretion disk. For the rays coming from below the point, this intensity would represent the specific intensity from the accretion disk below our flare model space. This was taken to be the Planck function at the temperature at the bottom or side of the model space, but in our calculations we are not including these factors. In our calculations the temperature of the atmosphere outside the model space is set to be 6000 K. Figure 4.6 illustrates two rays approaching a point in the model space from opposite directions.

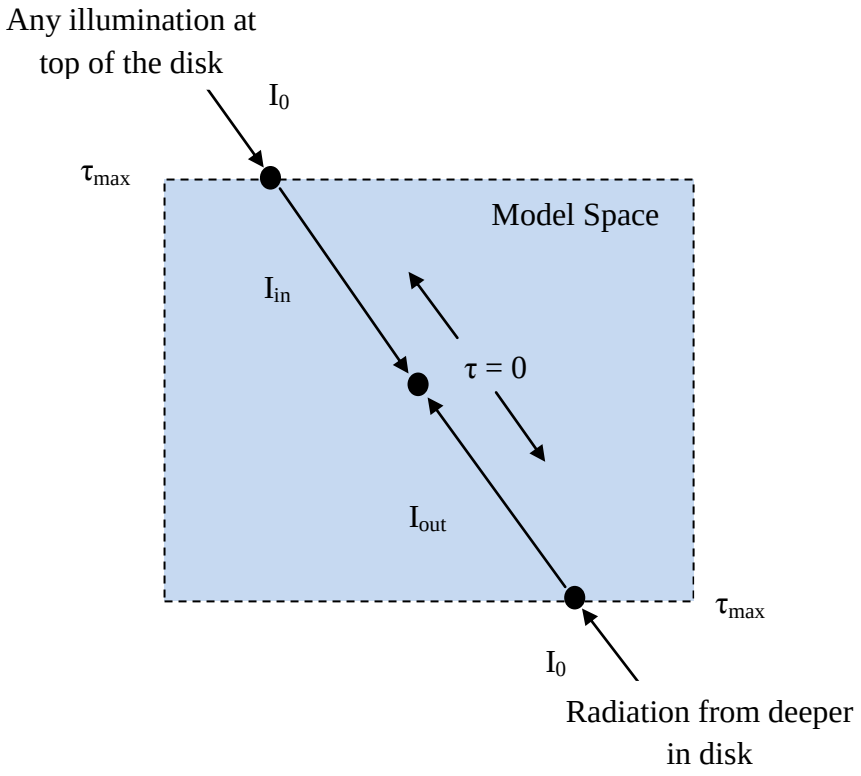

Figure 4.6. Radiation moving along inward and outward rays.

The radiative transfer calculation was tested in two ways. Our first test was a plane-parallel, isothermal atmosphere. We calculated the specific intensity leaving the atmosphere at different angles to the normal, and found them equal to the plank function, as expected. Our second test was a plane-parallel, solar photosphere model. Our output spectrum was consistent with the solar spectrum without absorption lines. We were also able to reproduce the correct limb darkening effect.

CHAPTER V

NON-LTE RADIATIVE TRANSFER PROGRAM

5.1 Non-LTE Radiative Transfer Program

The non-LTE radiative transfer program used in this work was originally developed by Williams and Shipman (1988). In its original form it assumed a plane-parallel geometry, and only treated the hydrogen lines in non-LTE. Non-LTE means that the level populations for a particular atom (i.e. number density of atoms with an electron in each particular level) are calculated explicitly by setting up the rate equations for transitions into and out of each level. The level populations for all other atoms are treated by assuming Thermodynamic equilibrium locally; which means using the Saha equation (2.2), and the Boltzmann equation (2.3). The program was extended to include the non-LTE treatment of helium lines by Nguyen (1993). Later, the program was used by Howland (1995) to study the absolute visual magnitudes, and line emission strengths from various accretion disk models.

5.1.1 LTE versus Non-LTE

In order to understand the non-LTE approach we have to know the thermodynamic equilibrium approach first. In Thermodynamic equilibrium (TE) there are four assumptions; (1) the degree of ionization is given by the Saha equation, (2) the level populations of atoms are given by Boltzmann's equation, (3) the mean intensity of radiation at any point is given by Planck's function ( ), and (4) ion and electron velocities are given by the Maxwell-Boltzmann velocity distribution. Thermodynamic equilibrium (TE) is a good approximation deep inside an atmosphere if the temperature is

constant over several photon mean-free-paths. It does not give good results near the surface of an atmosphere, due to the fact that temperature changes over a photon mean-free-path. A better approximation for an atmosphere is called LTE (Local Thermodynamic Equilibrium). In LTE assumptions (1), (2) and (4) are used, and the radiation field is calculated from the transfer equation instead of Planck's function. This is simple, but does not give a self-consistent solution. When LTE becomes unreliable another method is used. This is known as the Non-LTE approximations, and here only assumption (4) is kept. In non-LTE we seek to find the level populations of the atoms, and the radiation field, at each point self-consistently.

In the Non-LTE approach we begin with some estimate of the level populations of the atoms. This may be the thermodynamic equilibrium level populations, or level populations from a previous model. We then set the absorption coefficient ( ), the emission coefficient ( ), and the source function — , at each depth, and each frequency in the atmosphere. The radiation field is found by solving the radiative transfer equation using a technique like the Feautrier method (see section 4.2.1). Once the mean intensity of radiation is found at each depth, and each frequency, the rate equations for electron transitions into and out of each atomic level are calculated. These equations are solved to give new level populations. The entire process is repeated in iteration until some degree of convergence is reached.

5.1.2 Solving For Level Populations

To find level populations for hydrogen and helium we need to study the processes which take electrons out of the levels, and processes which put electrons into the levels.

In the radiative transfer program we consider 30 levels for hydrogen, with levels n = 1-5 broken into L-substates, and n = 6-20 treated as single levels. We, also, consider 27 levels for helium with n = 1-5, which are broken into L-substates. The transition rate equations are set up for all of these processes for H and He level populations (given in chapter 2) and rate equations are solved by Gaussian elimination. To find the level population (N_i) for each particular level (i), the steady state condition must be satisfied. This states that the sum of the transition rates for all collisional (C_i) and radiative (R_i) processes into and out of level i must be equal to zero. This can be written as

— (5.1)

Using the rates for the different processes from chapter 2, equation (5.1) can be written as,

— (Photo-ionization)

(Radiative-recombination)

(Collisional ionization)

(Three-body recombination)

(Collisions out of level i)

(Collisions into level i)

(Radiative transition out of level i)

(Radiative transition into level i) (5.2)

where the positive sign is for rates into level i, and negative sign is for rates out of level i. Thus, according to steady state condition, this differential equation (5.2) must be equal to zero. We have 30 such equations for hydrogen, and 27 equations for helium I. For each atom we also have an ionized state. Writing a rate equation similar to equation 5.1 for each ionized state would not produce a linearly independent equation. Instead, our final equation must state that the total of each bound level, plus the ionized state, must equal the total number density of that atom. We can write these equations into a matrix form as given below

$$\begin{vmatrix} \frac{dN_1}{dt} \\ \frac{dN_2}{dt} \\ \frac{dN_3}{dt} \\ \cdot \\ \cdot \\ \cdot \\ N_T \end{vmatrix} = \begin{vmatrix} a_{1,1} & a_{1,2} & a_{1,3} & . & . & . & . & a_{1,28} \\ a_{2,1} & & & & & & & \\ a_{3,1} & & & & & & & \\ . & & & & & & & \\ . & & & & & & & \\ . & & & & & & & \\ 1 & 1 & 1 & . & . & . & . & 1 \end{vmatrix} \begin{vmatrix} N_1 \\ N_2 \\ N_3 \\ . \\ . \\ . \\ N_+ \end{vmatrix} . \qquad (5.3)$$

Now we can solve this system of simultaneous equations by using the Gaussian elimination method to calculate the level populations.

The level population calculation was tested using the assumption of thermodynamic equilibrium. In this test we started with the level populations given by the Saha and Boltzmann equations, the radiation field was given by the Plank function at the local temperature, and the escape probabilities were set to zero. After calculating new level populations, we found the change in level populations to be very small, as expected.

5.2 Changes to Radiative Transfer Program

In my research project we made extensive modifications in the radiative transfer program. Instead of a plane-parallel atmosphere, we considered the atmosphere as non plane-parallel. Now the calculations are done in 2D; temperature T (z, r), density ρ (z, r), optical depth τ (z, r), mean intensity at frequency (ν), (z, r), and level populations of an atomic species i and level j $N_{i,j}$(z, r) are functions of vertical depth, and radial distance from the center of our flare model space. In our calculations the model space has cylindrical symmetry. We divide the vertical height into 50 depth steps (along z) and radial distance into 30 radial steps (along r) from the central axis to the edge of the cylinder. This required major modifications to the program. It was necessary to (1) change many arrays to two dimensions throughout the program, (2) change single do-loops over vertical distance into nested do-loops over vertical distance and radial distance, and (3) change the structure of many intermediate files used by the program.

As described in Chapter II, we made new tables of collision strengths from CMFGEN and Chianti. The collision strengths were stored in the program as 5th order polynomial fits of the logarithm of the collision strength versus the logarithm of the temperature. The collision strengths were converted into collision rates for each transition at the required temperature, as needed in the program.

As described in Chapter IV, the calculation of the radiation field needed significant change. As the model is no longer plane-parallel, we were not able to use the Feautrier method. In our calculations we have to find the specific intensity of incoming and outgoing radiation at 1500 (50 along z and 30 along r) points in the model space and at each point we consider six altitude angles (θ) and twelve azimuthal angles (Φ). We have

to calculate radiative transfer along 72-rays at each (z, r) point in our model space. Doing this provides us with the mean intensity at each point (as discussed in Chapter IV).

5.3 Calculating the line strengths

We also calculate the total line emission from the model space. To get emitted line strength, we first find the escape probability for line photons. We calculate the escape probability along the 72 rays. We use approximate Stark line profiles $\Phi_\nu(T, \rho)$, having Gaussian core and power law wings shown below.

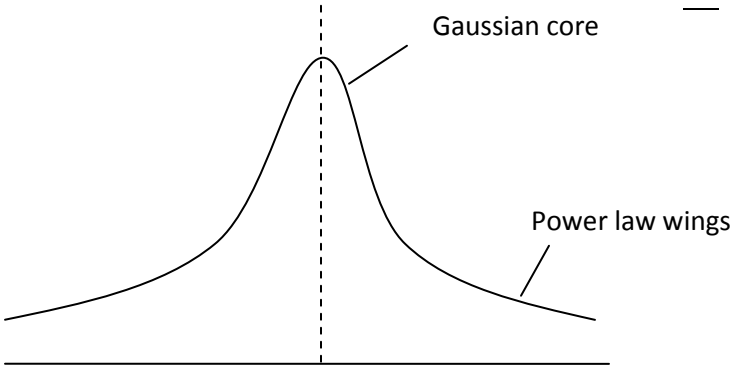

Figure 5.1. Stark Profile at a point

The approximate profiles are set to reflect published Stark profile for hydrogen. They depend on density and temperature. The profiles are normalized so that when integrated over frequency, the result is unity.

(5.3)

Each profile is interpolated to 48 frequency points across the line profile, within the range (Doppler widths). These points were chosen to be the abscissa a

Gaussian numerical integration. In terms of the numerical integration, equation 5.3 becomes

(5.4)

where the w_j are the Gaussian weights.

Then we calculate the optical depth (τ) along each ray for each Gaussian frequency point in the line profile. Also, the opacity at a point is set by the Stark profile ($\varphi_v(T, \rho)$) at each point along the ray. If the gas along the ray has a radial velocity relative to the point in question, the profiles are shifted in frequency by the Doppler formula, given as

— (5.5)

where is the change in velocity. The escape probability along a single ray is

. (5.6)

If , then $P_{esc} = 1$, and if , then P_{esc} goes to 0. The escape probability along 72 rays is given by

— (5.7)

here, the w_i are the angular Gaussian weights.

Once the escape probability for a particular line photon is calculated, the rate at which those photons leave the atmosphere from one point is, . This expression must be integrated over the entire volume of our flare model space. In addition, to find just the line emission caused by the flare, we must subtract off the line emission from the unperturbed atmosphere. For this calculation, the temperature and density in the unperturbed atmosphere is used, along with the assumption that the level populations are

in thermodynamic equilibrium. As the temperature in the unperturbed atmosphere was assumed to be low ( ), the rate of hydrogen line emission would be low.

5.4 How the Program Works

When the program begins execution, it is initialized in the subroutine called "INIT", where we read in the data files, and various arrays are set. If we chose to start the calculation in thermodynamic equilibrium (T.E.), we used the Saha equation to find the degree of ionization, and Boltzmann equation to set the level population for hydrogen and helium. The Planck function was used to set the initial radiation field in T.E. We read in the escape probability table, which gives us the escape probability of photons based on line optical depth and continuous optical depth.

If we chose to start a model with the level populations and the radiation field taken from a previous model, we read in the H and He level populations and mean intensity, storing the values into arrays, which allows for later access. We set the continuous opacity (κ), emissivity (j) and source function (S) at the 50 depths (z), the 30 radial distances (r), and the 75 continuum frequencies. As already discussed, we found the mean intensity of radiation at each point (z, r) and at all 75 frequencies by solving the radiative transfer equation along 72 rays.

After that we wanted to solve for new level populations. To set up the rate equations we first needed to set all the rate coefficients. These are (1) the photoionization and radiative recombination rates, (2) the collisional excitation and de-excitation rates, (3) the collisional ionization and three-body recombination rates, and (4) the line photon escape probabilities. These are set as described in chapter 2. The rate equations for hydrogen and helium level populations are solved using Gaussian elimination.

Once the new levels populations found, we then start iterating. The new level populations allowed us to find new estimates of the mean intensity at each point. This process was repeated for about 40 iterations to obtain level populations with a sufficiently small deviation. Generally, it was felt that the model was sufficiently converged when the change in each level population per iteration was less than 0.1 %. Running a model through 40 iterations would take 3-4 hours on our IRAF workstation. If a model was not sufficiently converged after one run, we started it again for another 40 iterations.

Before exiting the program all system variable were store in direct-access files. These included all level populations for hydrogen and helium, and the mean intensity of radiation at each point, and each frequency. Following on the next page is a flowchart showing the full procedure. Appendix D gives a summary of the major subroutines in the radiative transfer program.

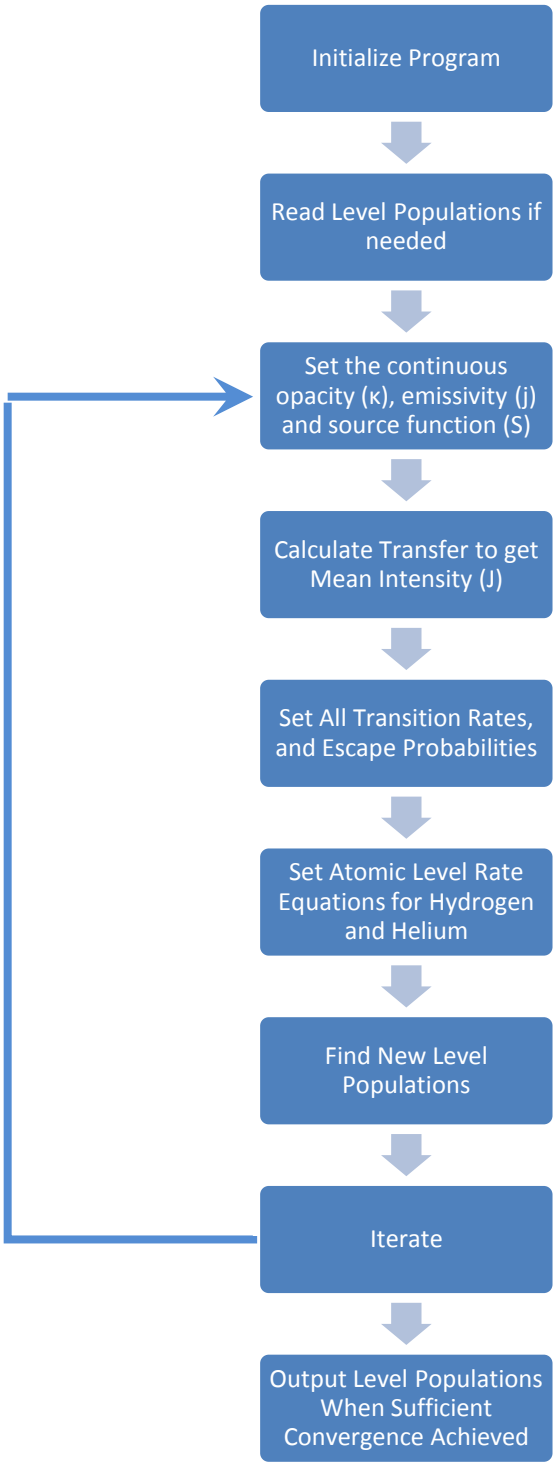

Figure 5.2. Flow chart for the non-LTE radiative transfer program

CHAPTER VI

RESULTS

6.1 Our Line Strengths

As part of the research, we calculated different line strengths in the Hydrogen series. These values were calculated from the flare models developed by Jeewoo. Listed in the tables below are theses values as well as the ratios of H-alpha to H-beta and H-gamma to H-beta. The model numbers correspond to the same model number in Jeewoo's thesis (Park, 2010). The difference between the models themselves is in the flux and magnetic field strength being changed. The length of time represents how long the flux of gas was heated. Model 1 has a flux of 1.00×10^{7} (J m^{-2} s^{-1}) and a magnetic field of 50 gauss. Model 3 has a flux of 1.00×10^{7} (J m^{-2} s^{-1}) and a magnetic field of 150 gauss. Model 4 has a flux of 1.00×10^{6} (J m^{-2} s^{-1}) and a magnetic field of 50 gauss.

Table 6.1 Our computed line strengths from Park's model 4.

Model 4					
Time (s)	Hβ	Hα/Hβ	Hγ/Hβ	Hδ/Hg	Electron density
0.5	3.23E+14	2.47	0.52	0.60	6.98E+11
1.0	5.17E+14	3.19	0.49	0.58	7.30E+11
1.5	5.12E+14	2.85	0.49	0.59	7.07E+11
2.0	4.91E+14	2.68	0.50	0.59	6.96E+11
2.5	4.95E+14	2.69	0.49	0.59	6.97E+11
3.0	4.99E+14	2.70	0.49	0.59	6.96E+11
3.5	7.22E+14	2.82	0.48	0.58	7.35E+11
4.0	7.41E+14	2.88	0.48	0.58	7.40E+11
4.5	7.41E+14	2.86	0.48	0.58	7.38E+11
5.0	7.52E+14	2.88	0.48	0.58	7.39E+11

Table 6.2 Our computed line strengths from Park's model 3.

Model 3					
Time (s)	Hβ	Hα/Hβ	Hγ/Hβ	Hδ/Hg	Electron density
0.5	1.20E+15	3.59	0.45	0.56	8.18E+11
1.0	9.79E+14	3.35	0.46	0.57	7.85E+11
1.5	3.34E+14	0.57	0.53	0.63	3.69E+11
2.0	1.86E+14	-1.89	0.62	0.68	1.71E+11
2.5	1.33E+14	-2.40	0.64	0.70	1.65E+11
3.0	8.30E+13	-5.68	0.75	0.74	1.61E+11

Table 6.3 Our computed line strengths from Park's model 1.

Model 1					
Time (s)	Hβ	Hα/Hβ	Hγ/Hβ	Hδ/Hg	Electron density
0.5	4.19E+15	4.31	0.42	0.53	1.12E+12
1.0	6.66E+15	4.45	0.41	0.52	1.27E+12
1.5	7.02E+15	4.38	0.41	0.52	1.30E+12
2.0	6.76E+15	4.34	0.41	0.52	1.24E+12
2.5	3.18E+15	4.34	0.43	0.53	9.14E+11
3.0	2.73E+15	4.08	0.43	0.54	7.76E+11

The computed line strengths for , , and for these three models are shown in Figure 6.1

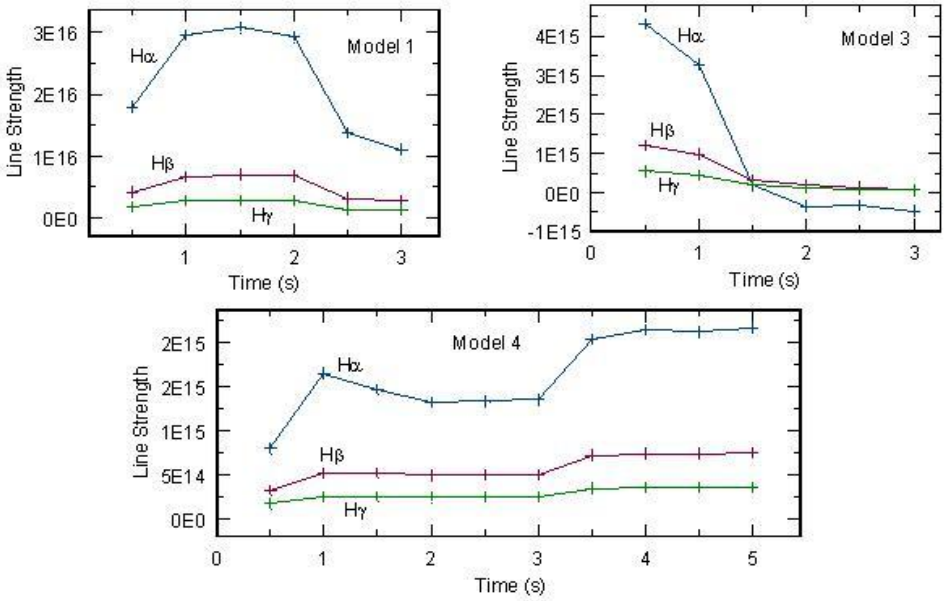

Figure 6.1. Balmer line strengths (ergs s^{-1}) for 3 J. Park flare models.

6.2 Comparison with Observations

References to flare spectra with line strengths are hard to find in the literature. This is probably due to the fact that observing a flare is a serendipitous event. In many cases of spectra that do exist, the spectra cover the blue and near ultraviolet, or they cover the near infrared. Donati-Falchi, et.al, (1984a, 1984b) observed a white light flare on June 4, 1980. A series of spectra were taken with the spectrograph slit running across the flare footpoint. For each spectrum a series of 6 tracings, along the slit, ran from the bottom of the footpoint to the top. The total line and continuous emission was estimated from the flare footpoint by assuming a circular symmetry in the footpoint, and by assuming that the emission was isotropic. The table below gives the wavelength-integrated line intensity for at the center of the footpoint. Also given are the Balmer decrements and . The Balmer decrements are near unity, indicating that the emitting gas was optically thick in the Balmer lines, and the temperature was of the order of K.

Table 6.4 The flare line strengths observed by Donati-Falchi, et.al. (1984b)

Spectrum No.	Time UT	Integrated Intensity		
3	22:59:50	704.0	0.654	1.180
5	23:01:10	345.4	1.249	1.113
6	23:01:46	250.0	0.679	0.998
8	23:04:05	44.7	0.955	1.164
9	23:04:47	86.5	0.824	0.907

We compared these values with our results and found that the Balmer decrements in our case are not close to unity. This implies that the atmosphere is optically thin for

Balmer lines in our models. It means that the Park flare models are not going deep enough into the disk of CVs.

Neidig and Wiborg (1984) obtained spectra for 3 white light flares on 24 April 1981, 4 June 1982, and 6 June 1982. Unfortunately, the spectra were either in the violet/UV (3600 – 4000 A^o), or in the near infrared (8000 – 9000 A^o), and did not cover the lower hydrogen Balmer lines. The electron density in the line emitting region of the flares is estimated using either the line widths (full width at half maximum), or the Inglis-Teller formula which relates electron density with the highest resolvable Balmer line. For the 24 April flare they found an electron density of based on a 5 Å half-width for the H_{15} Balmer line. For the 4 June flare they found the highest resolved Balmer line to be H_{17}, and using the Inglis-Teller formula gave an electron density of . The flare of 6 June was more noisy, but the line widths were similar to the flare of 24 April.

In our results we found that maximum electron density is at . At this temperature we get strong Balmer line emission. Temperatures were higher at greater height in the flare, but the gas density was less, so the amount of Balmer line emission from these regions was less. The electron density estimates of Neidig and Wiborg are roughly 20 times larger than ours. This, again, indicates that the flare models of Park did not extend as deep into the disk, as actual solar flares. The reason for this is not known.

6.3 Future Work

In our calculations of emission lines, from the solar-type flares on accretion disks, we found disagreements with previously published results. In order to settle this disagreement more work will need to be completed. One of these is to run more models from Jeewoo's research work. Another is to update and change some of the codes used in modeling the solar-type flares from Jeewoo Park's work.

APPENDICES

APPENDIX A

HYDROGEN COLLISION STRENGTH REFERENCES

Lower Level	Upper Level	Source	Lower Level	Upper Level	Source	Lower Table	Upper Level	Source
1-s	2-s	Chianti	2-s	5-g	Chianti	2-p	n=19	CMFGEN
1-s	2-p	Chianti	2-s	n=6	CMFGEN	2-p	n=20	CMFGEN
1-s	3-s	Chianti	2-s	n=7	CMFGEN			
1-s	3-p	Chianti	2-s	n=8	CMFGEN	3-s	3-p	Brock
1-s	3-d	Chianti	2-s	n=9	CMFGEN	3-s	3-d	Zero
1-s	4-s	Chianti	2-s	n=10	CMFGEN	3-s	4-s	CMFGEN
1-s	4-p	Chianti	2-s	n=11	CMFGEN	3-s	4-p	CMFGEN
1-s	4-d	Chianti	2-s	n=12	CMFGEN	3-s	4-d	CMFGEN
1-s	4-f	Chianti	2-s	n=13	CMFGEN	3-s	4-f	CMFGEN
1-s	5-s	Chianti	2-s	n=14	CMFGEN	3-s	5-s	CMFGEN
1-s	5-p	Chianti	2-s	n=15	CMFGEN	3-s	5-p	Johns
1-s	5-d	Chianti	2-s	n=16	CMFGEN	3-s	5-d	Johns
1-s	5-f	Chianti	2-s	n=17	CMFGEN	3-s	5-f	Johns
1-s	5-g	Chianti	2-s	n=18	CMFGEN	3-s	5-g	Johns
1-s	n=6	CMFGEN	2-s	n=19	CMFGEN	3-s	n=6	CMFGEN
1-s	n=7	CMFGEN	2-s	n=20	CMFGEN	3-s	n=7	CMFGEN
1-s	n=8	CMFGEN				3-s	n=8	CMFGEN
1-s	n=9	CMFGEN	2-p	3-s	Chianti	3-s	n=9	CMFGEN
1-s	n=10	CMFGEN	2-p	3-p	Chianti	3-s	n=10	CMFGEN
1-s	n=11	CMFGEN	2-p	3-d	Chianti	3-s	n=11	CMFGEN
1-s	n=12	CMFGEN	2-p	4-s	CMFGEN	3-s	n=12	CMFGEN
1-s	n=13	CMFGEN	2-p	4-p	CMFGEN	3-s	n=13	CMFGEN
1-s	n=14	CMFGEN	2-p	4-d	CMFGEN	3-s	n=14	CMFGEN
1-s	n=15	CMFGEN	2-p	4-f	CMFGEN	3-s	n=15	CMFGEN
1-s	n=16	CMFGEN	2-p	5-s	CMFGEN	3-s	n=16	CMFGEN
1-s	n=17	CMFGEN	2-p	5-p	Johns	3-s	n=17	CMFGEN
1-s	n=18	CMFGEN	2-p	5-d	Johns	3-s	n=18	CMFGEN
1-s	n=19	CMFGEN	2-p	5-f	Johns	3-s	n=19	CMFGEN
1-s	n=20	CMFGEN	2-p	5-g	Johns	3-s	n=20	CMFGEN
			2-p	n=6	CMFGEN			
2-s	2-p	Brock	2-p	n=7	CMFGEN	3-p	3-d	Brock
2-s	3-s	Chianti	2-p	n=8	CMFGEN	3-p	4-s	CMFGEN
2-s	3-p	Chianti	2-p	n=9	CMFGEN	3-p	4-p	CMFGEN
2-s	3-d	Chianti	2-p	n=10	CMFGEN	3-p	4-d	CMFGEN
2-s	4-s	Chianti	2-p	n=11	CMFGEN	3-p	4-f	CMFGEN
2-s	4-p	Chianti	2-p	n=12	CMFGEN	3-p	5-s	CMFGEN
2-s	4-d	Chianti	2-p	n=13	CMFGEN	3-p	5-p	Johns
2-s	4-f	Chianti	2-p	n=14	CMFGEN	3-p	5-d	Johns
2-s	5-s	Chianti	2-p	n=15	CMFGEN	3-p	5-f	Johns
2-s	5-p	Chianti	2-p	n=16	CMFGEN	3-p	5-g	Johns
2-s	5-d	Chianti	2-p	n=17	CMFGEN	3-p	n=6	CMFGEN
2-s	5-f	Chianti	2-p	n=18	CMFGEN	3-p	n=7	CMFGEN

Lower Level	Upper Level	Source	Lower Level	Upper Level	Source	Lower Table	Upper Level	Source
3-p	n=8	CMFGEN	4-s	5-s	CMFGEN	4-p	n=20	CMFGEN
3-p	n=9	CMFGEN	4-s	5-p	Johns			
3-p	n=10	CMFGEN	4-s	5-d	Johns	4-d	4-f	Brock
3-p	n=11	CMFGEN	4-s	5-f	Johns	4-d	5-s	CMFGEN
3-p	n=12	CMFGEN	4-s	5-g	Johns	4-d	5-p	Johns
3-p	n=13	CMFGEN	4-s	n=6	CMFGEN	4-d	5-d	Johns
3-p	n=14	CMFGEN	4-s	n=7	CMFGEN	4-d	5-f	Johns
3-p	n=15	CMFGEN	4-s	n=8	CMFGEN	4-d	5-g	Johns
3-p	n=16	CMFGEN	4-s	n=9	CMFGEN	4-d	n=6	CMFGEN
3-p	n=17	CMFGEN	4-s	n=10	CMFGEN	4-d	n=7	CMFGEN
3-p	n=18	CMFGEN	4-s	n=11	CMFGEN	4-d	n=8	CMFGEN
3-p	n=19	CMFGEN	4-s	n=12	CMFGEN	4-d	n=9	CMFGEN
3-p	n=20	CMFGEN	4-s	n=13	CMFGEN	4-d	n=10	CMFGEN
			4-s	n=14	CMFGEN	4-d	n=11	CMFGEN
3-d	4-s	CMFGEN	4-s	n=15	CMFGEN	4-d	n=12	CMFGEN
3-d	4-p	CMFGEN	4-s	n=16	CMFGEN	4-d	n=13	CMFGEN
3-d	4-d	CMFGEN	4-s	n=17	CMFGEN	4-d	n=14	CMFGEN
3-d	4-f	CMFGEN	4-s	n=18	CMFGEN	4-d	n=15	CMFGEN
3-d	5-s	CMFGEN	4-s	n=19	CMFGEN	4-d	n=16	CMFGEN
3-d	5-p	Johns	4-s	n=20	CMFGEN	4-d	n=17	CMFGEN
3-d	5-d	Johns				4-d	n=18	CMFGEN
3-d	5-f	Johns	4-p	4-d	Brock	4-d	n=19	CMFGEN
3-d	5-g	Johns	4-p	4-f	Zero	4-d	n=20	CMFGEN
3-d	n=6	CMFGEN	4-p	5-s	CMFGEN			
3-d	n=7	CMFGEN	4-p	5-p	Johns	4-f	5-s	CMFGEN
3-d	n=8	CMFGEN	4-p	5-d	Johns	4-f	5-p	Johns
3-d	n=9	CMFGEN	4-p	5-f	Johns	4-f	5-d	Johns
3-d	n=10	CMFGEN	4-p	5-g	Johns	4-f	5-f	Johns
3-d	n=11	CMFGEN	4-p	n=6	CMFGEN	4-f	5-g	Johns
3-d	n=12	CMFGEN	4-p	n=7	CMFGEN	4-f	n=6	CMFGEN
3-d	n=13	CMFGEN	4-p	n=8	CMFGEN	4-f	n=7	CMFGEN
3-d	n=14	CMFGEN	4-p	n=9	CMFGEN	4-f	n=8	CMFGEN
3-d	n=15	CMFGEN	4-p	n=10	CMFGEN	4-f	n=9	CMFGEN
3-d	n=16	CMFGEN	4-p	n=11	CMFGEN	4-f	n=10	CMFGEN
3-d	n=17	CMFGEN	4-p	n=12	CMFGEN	4-f	n=11	CMFGEN
3-d	n=18	CMFGEN	4-p	n=13	CMFGEN	4-f	n=12	CMFGEN
3-d	n=19	CMFGEN	4-p	n=14	CMFGEN	4-f	n=13	CMFGEN
3-d	n=20	CMFGEN	4-p	n=15	CMFGEN	4-f	n=14	CMFGEN
			4-p	n=16	CMFGEN	4-f	n=15	CMFGEN
4-s	4-p	Brock	4-p	n=17	CMFGEN	4-f	n=16	CMFGEN
4-s	4-d	Zero	4-p	n=18	CMFGEN	4-f	n=17	CMFGEN
4-s	4-f	Zero	4-p	n=19	CMFGEN	4-f	n=18	CMFGEN

Lower Level	Upper Level	Source	Lower Level	Upper Level	Source	Lower Table	Upper Level	Source
4-f	n=19	CMFGEN	5-d	5-f	CMFGEN	5-g	n=13	Johns
4-f	n=20	CMFGEN	5-d	5-g	Johns	5-g	n=14	Johns
			5-d	n=6	Johns	5-g	n=15	Johns
5-s	5-p	Brock	5-d	n=7	Johns	5-g	n=16	Johns
5-s	5-d	Zero	5-d	n=8	Johns	5-g	n=17	Johns
5-s	5-f	Zero	5-d	n=9	CMFGEN	5-g	n=18	Johns
5-s	5-g	Zero	5-d	n=10	Johns	5-g	n=19	Johns
5-s	n=6	CMFGEN	5-d	n=11	Johns	5-g	n=20	Johns
5-s	n=7	CMFGEN	5-d	n=12	Johns			
5-s	n=8	CMFGEN	5-d	n=13	Johns	n=6	n=7	CMFGEN
5-s	n=9	CMFGEN	5-d	n=14	Johns	n=6	n=8	CMFGEN
5-s	n=10	CMFGEN	5-d	n=15	Johns	n=6	n=9	CMFGEN
5-s	n=11	CMFGEN	5-d	n=16	Johns	n=6	n=10	CMFGEN
5-s	n=12	CMFGEN	5-d	n=17	Johns	n=6	n=11	CMFGEN
5-s	n=13	CMFGEN	5-d	n=18	Johns	n=6	n=12	CMFGEN
5-s	n=14	CMFGEN	5-d	n=19	Johns	n=6	n=13	CMFGEN
5-s	n=15	CMFGEN	5-d	n=20	Johns	n=6	n=14	CMFGEN
5-s	n=16	CMFGEN				n=6	n=15	CMFGEN
5-s	n=17	CMFGEN	5-f	5-g	Brock	n=6	n=16	CMFGEN
5-s	n=18	CMFGEN	5-f	n=6	Johns	n=6	n=17	CMFGEN
5-s	n=19	CMFGEN	5-f	n=7	Johns	n=6	n=18	CMFGEN
5-s	n=20	CMFGEN	5-f	n=8	Johns	n=6	n=19	CMFGEN
			5-f	n=9	Johns	n=6	n=20	CMFGEN
5-p	5-d	Brock	5-f	n=10	Johns			
5-p	5-f	Zero	5-f	n=11	Johns	n=7	n=8	CMFGEN
5-p	5-g	Zero	5-f	n=12	Johns	n=7	n=9	CMFGEN
5-p	n=6	Johns	5-f	n=13	Johns	n=7	n=10	CMFGEN
5-p	n=7	Johns	5-f	n=14	Johns	n=7	n=11	CMFGEN
5-p	n=8	Johns	5-f	n=15	Johns	n=7	n=12	CMFGEN
5-p	n=9	Johns	5-f	n=16	Johns	n=7	n=13	CMFGEN
5-p	n=10	Johns	5-f	n=17	Johns	n=7	n=14	CMFGEN
5-p	n=11	Johns	5-f	n=18	Johns	n=7	n=15	CMFGEN
5-p	n=12	Johns	5-f	n=19	Johns	n=7	n=16	CMFGEN
5-p	n=13	Johns	5-f	n=20	Johns	n=7	n=17	CMFGEN
5-p	n=14	Johns				n=7	n=18	CMFGEN
5-p	n=15	Johns	5-g	n=6	Johns	n=7	n=19	CMFGEN
5-p	n=16	Johns	5-g	n=7	Johns	n=7	n=20	CMFGEN
5-p	n=17	Johns	5-g	n=8	Johns			
5-p	n=18	Johns	5-g	n=9	Johns	n=8	n=9	CMFGEN
5-p	n=19	Johns	5-g	n=10	Johns	n=8	n=10	CMFGEN
5-p	n=20	Johns	5-g	n=11	Johns	n=8	n=11	CMFGEN
			5-g	n=12	Johns	n=8	n=12	CMFGEN

Lower Level	Upper Level	Source	Lower Level	Upper Level	Source	Lower Table	Upper Level	Source
n=8	n=13	CMFGEN	n=12	n=13	CMFGEN	n=19	n=20	CMFGEN
n=8	n=14	CMFGEN	n=12	n=14	CMFGEN			
n=8	n=15	CMFGEN	n=12	n=15	CMFGEN			
n=8	n=16	CMFGEN	n=12	n=16	CMFGEN			
n=8	n=17	CMFGEN	n=12	n=17	CMFGEN			
n=8	n=18	CMFGEN	n=12	n=18	CMFGEN			
n=8	n=19	CMFGEN	n=12	n=19	CMFGEN			
n=8	n=20	CMFGEN	n=12	n=20	CMFGEN			
n=9	n=10	CMFGEN	n=13	n=14	CMFGEN			
n=9	n=11	CMFGEN	n=13	n=15	CMFGEN			
n=9	n=12	CMFGEN	n=13	n=16	CMFGEN			
n=9	n=13	CMFGEN	n=13	n=17	CMFGEN			
n=9	n=14	CMFGEN	n=13	n=18	CMFGEN			
n=9	n=15	CMFGEN	n=13	n=19	CMFGEN			
n=9	n=16	CMFGEN	n=13	n=20	CMFGEN			
n=9	n=17	CMFGEN						
n=9	n=18	CMFGEN	n=14	n=15	CMFGEN			
n=9	n=19	CMFGEN	n=14	n=16	CMFGEN			
n=9	n=20	CMFGEN	n=14	n=17	CMFGEN			
			n=14	n=18	CMFGEN			
n=10	n=11	CMFGEN	n=14	n=19	CMFGEN			
n=10	n=12	CMFGEN	n=14	n=20	CMFGEN			
n=10	n=13	CMFGEN						
n=10	n=14	CMFGEN	n=15	n=16	CMFGEN			
n=10	n=15	CMFGEN	n=15	n=17	CMFGEN			
n=10	n=16	CMFGEN	n=15	n=18	CMFGEN			
n=10	n=17	CMFGEN	n=15	n=19	CMFGEN			
n=10	n=18	CMFGEN	n=15	n=20	CMFGEN			
n=10	n=19	CMFGEN						
n=10	n=20	CMFGEN	n=16	n=17	CMFGEN			
			n=16	n=18	CMFGEN			
n=11	n=12	CMFGEN	n=16	n=19	CMFGEN			
n=11	n=13	CMFGEN	n=16	n=20	CMFGEN			
n=11	n=14	CMFGEN						
n=11	n=15	CMFGEN	n=17	n=18	CMFGEN			
n=11	n=16	CMFGEN	n=17	n=19	CMFGEN			
n=11	n=17	CMFGEN	n=17	n=20	CMFGEN			
n=11	n=18	CMFGEN						
n=11	n=19	CMFGEN	n=18	n=19	CMFGEN			
n=11	n=20	CMFGEN	n=18	n=20	CMFGEN			

APPENDIX B

HELIUM COLLISION STRENGTH REFERENCES

Lower Level	Upper Level	Source	Lower Level	Upper Level	Source	Lower Table	Upper Level	Source
1-1s	2-1s	Chianti	2-1s	3-3p	CMFGEN	3-1s	5-1s	
1-1s	2-1p	Chianti	2-1s	3-3d	CMFGEN	3-1s	5-1p	
1-1s	3-1s	Chianti	2-1s	4-3s	CMFGEN	3-1s	5-1d	
1-1s	3-1p	CMFGEN	2-1s	4-3p	CMFGEN	3-1s	5-1f	
1-1s	3-1d	Chianti	2-1s	4-3d	CMFGEN	3-1s	2-3s	CMFGEN
1-1s	4-1s	Chianti	2-1s	4-3f	CMFGEN	3-1s	2-3p	CMFGEN
1-1s	4-1p	CMFGEN	2-1s	5-3s		3-1s	3-3s	CMFGEN
1-1s	4-1d	Chianti	2-1s	5-3p		3-1s	3-3p	CMFGEN
1-1s	4-1f	Chianti	2-1s	5-3d		3-1s	3-3d	CMFGEN
1-1s	5-1s	Chianti	2-1s	5-3f		3-1s	4-3s	CMFGEN
1-1s	5-1p					3-1s	4-3p	CMFGEN
1-1s	5-1d	Chianti	2-1p	3-1s	CMFGEN	3-1s	4-3d	CMFGEN
1-1s	5-1f	Chianti	2-1p	3-1p	CMFGEN	3-1s	4-3f	CMFGEN
1-1s	2-3s	Chianti	2-1p	3-1d	CMFGEN	3-1s	5-3s	
1-1s	2-3p	Chianti	2-1p	4-1s	CMFGEN	3-1s	5-3p	
1-1s	3-3s	Chianti	2-1p	4-1p	CMFGEN	3-1s	5-3d	
1-1s	3-3p	Chianti	2-1p	4-1d	CMFGEN	3-1s	5-3f	
1-1s	3-3d	Chianti	2-1p	4-1f	CMFGEN			
1-1s	4-3s	Chianti	2-1p	5-1s		3-1p	3-1d	CMFGEN
1-1s	4-3p	Chianti	2-1p	5-1p		3-1p	4-1s	CMFGEN
1-1s	4-3d	Chianti	2-1p	5-1d		3-1p	4-1p	CMFGEN
1-1s	4-3f	Chianti	2-1p	5-1f		3-1p	4-1d	CMFGEN
1-1s	5-3s	Chianti	2-1p	2-3s	CMFGEN	3-1p	4-1f	CMFGEN
1-1s	5-3p		2-1p	2-3p	CMFGEN	3-1p	5-1s	
1-1s	5-3d		2-1p	3-3s	CMFGEN	3-1p	5-1p	
1-1s	5-3f		2-1p	3-3p	CMFGEN	3-1p	5-1d	
			2-1p	3-3d	CMFGEN	3-1p	5-1f	
2-1s	2-1p	CMFGEN	2-1p	4-3s	CMFGEN	3-1p	2-3s	CMFGEN
2-1s	3-1s	CMFGEN	2-1p	4-3p	CMFGEN	3-1p	2-3p	CMFGEN
2-1s	3-1p	CMFGEN	2-1p	4-3d	CMFGEN	3-1p	3-3s	CMFGEN
2-1s	3-1d	CMFGEN	2-1p	4-3f	CMFGEN	3-1p	3-3p	CMFGEN
2-1s	4-1s	CMFGEN	2-1p	5-3s		3-1p	3-3d	CMFGEN
2-1s	4-1p	CMFGEN	2-1p	5-3p		3-1p	4-3s	CMFGEN
2-1s	4-1d	CMFGEN	2-1p	5-3d		3-1p	4-3p	CMFGEN
2-1s	4-1f	CMFGEN	2-1p	5-3f		3-1p	4-3d	CMFGEN
2-1s	5-1s					3-1p	4-3f	CMFGEN
2-1s	5-1p		3-1s	3-1p	CMFGEN	3-1p	5-3s	
2-1s	5-1d		3-1s	3-1d	CMFGEN	3-1p	5-3p	
2-1s	5-1f		3-1s	4-1s	CMFGEN	3-1p	5-3d	
2-1s	2-3s	CMFGEN	3-1s	4-1p	CMFGEN	3-1p	5-3f	
2-1s	2-3p	CMFGEN	3-1s	4-1d	CMFGEN			
2-1s	3-3s	CMFGEN	3-1s	4-1f	CMFGEN	3-1d	4-1s	CMFGEN

Lower Level	Upper Level	Source	Lower Level	Upper Level	Source	Lower Table	Upper Level	Source
3-1d	4-1s	CMFGEN				4-1f	5-1d	
3-1d	4-1p	CMFGEN	4-1p	4-1d	CMFGEN	4-1f	5-1f	
3-1d	4-1d	CMFGEN	4-1p	4-1f	CMFGEN	4-1f	2-3s	CMFGEN
3-1d	4-1f	CMFGEN	4-1p	5-1s		4-1f	2-3p	CMFGEN
3-1d	5-1s		4-1p	5-1p		4-1f	3-3s	CMFGEN
3-1d	5-1p		4-1p	5-1d		4-1f	3-3p	CMFGEN
3-1d	5-1d		4-1p	5-1f		4-1f	3-3d	CMFGEN
3-1d	5-1f		4-1p	2-3s	CMFGEN	4-1f	4-3s	CMFGEN
3-1d	2-3s	CMFGEN	4-1p	2-3p	CMFGEN	4-1f	4-3p	CMFGEN
3-1d	2-3p	CMFGEN	4-1p	3-3s	CMFGEN	4-1f	4-3d	CMFGEN
3-1d	3-3s	CMFGEN	4-1p	3-3p	CMFGEN	4-1f	4-3f	CMFGEN
3-1d	3-3p	CMFGEN	4-1p	3-3d	CMFGEN	4-1f	5-3s	
3-1d	3-3d	CMFGEN	4-1p	4-3s	CMFGEN	4-1f	5-3p	
3-1d	4-3s	CMFGEN	4-1p	4-3p	CMFGEN	4-1f	5-3d	
3-1d	4-3p	CMFGEN	4-1p	4-3d	CMFGEN	4-1f	5-3f	
3-1d	4-3d	CMFGEN	4-1p	4-3f	CMFGEN			
3-1d	4-3f	CMFGEN	4-1p	5-3s		5-1s	5-1p	
3-1d	5-3s		4-1p	5-3p		5-1s	5-1d	
3-1d	5-3p		4-1p	5-3d		5-1s	5-1f	
3-1d	5-3d		4-1p	5-3f		5-1s	2-3s	
3-1d	5-3f					5-1s	2-3p	
			4-1d	4-1f	CMFGEN	5-1s	3-3s	
4-1s	4-1p	CMFGEN	4-1d	5-1s		5-1s	3-3p	
4-1s	4-1d	CMFGEN	4-1d	5-1p		5-1s	3-3d	
4-1s	4-1f	CMFGEN	4-1d	5-1d		5-1s	4-3s	
4-1s	5-1s		4-1d	5-1f		5-1s	4-3p	
4-1s	5-1p		4-1d	2-3s	CMFGEN	5-1s	4-3d	
4-1s	5-1d		4-1d	2-3p	CMFGEN	5-1s	4-3f	
4-1s	5-1f		4-1d	3-3s	CMFGEN	5-1s	5-3s	
4-1s	2-3s	CMFGEN	4-1d	3-3p	CMFGEN	5-1s	5-3p	
4-1s	2-3p	CMFGEN	4-1d	3-3d	CMFGEN	5-1s	5-3d	
4-1s	3-3s	CMFGEN	4-1d	4-3s	CMFGEN	5-1s	5-3f	
4-1s	3-3p	CMFGEN	4-1d	4-3p	CMFGEN			
4-1s	3-3d	CMFGEN	4-1d	4-3d	CMFGEN	5-1p	5-1d	
4-1s	4-3s	CMFGEN	4-1d	4-3f	CMFGEN	5-1p	5-1f	
4-1s	4-3p	CMFGEN	4-1d	5-3s		5-1p	2-3s	
4-1s	4-3d	CMFGEN	4-1d	5-3p		5-1p	2-3p	
4-1s	4-3f	CMFGEN	4-1d	5-3d		5-1p	3-3s	
4-1s	5-3s		4-1d	5-3f		5-1p	3-3p	
4-1s	5-3p					5-1p	3-3d	
4-1s	5-3d		4-1f	5-1s		5-1p	4-3s	
4-1s	5-3f		4-1f	5-1p		5-1p	4-3p	

Lower Level	Upper Level	Source	Lower Level	Upper Level	Source	Lower Table	Upper Level	Source
5-1p	4-3d		2-3s	4-3d	CMFGEN	3-3d	4-3d	CMFGEN
5-1p	4-3f		2-3s	4-3f	CMFGEN	3-3d	4-3f	CMFGEN
5-1p	5-3s		2-3s	5-3s		3-3d	5-3s	
5-1p	5-3p		2-3s	5-3p		3-3d	5-3p	
5-1p	5-3d		2-3s	5-3d		3-3d	5-3d	
5-1p	5-3f		2-3s	5-3f		3-3d	5-3f	
5-1d	5-1f		2-3p	3-3s	CMFGEN	4-3s	4-3p	CMFGEN
5-1d	2-3s		2-3p	3-3p	CMFGEN	4-3s	4-3d	CMFGEN
5-1d	2-3p		2-3p	3-3d	CMFGEN	4-3s	4-3f	CMFGEN
5-1d	3-3s		2-3p	4-3s	CMFGEN	4-3s	5-3s	
5-1d	3-3p		2-3p	4-3p	CMFGEN	4-3s	5-3p	
5-1d	3-3d		2-3p	4-3d	CMFGEN	4-3s	5-3d	
5-1d	4-3s		2-3p	4-3f	CMFGEN	4-3s	5-3f	
5-1d	4-3p		2-3p	5-3s				
5-1d	4-3d		2-3p	5-3p		4-3p	4-3d	CMFGEN
5-1d	4-3f		2-3p	5-3d		4-3p	4-3f	CMFGEN
5-1d	5-3s		2-3p	5-3f		4-3p	5-3s	
5-1d	5-3p					4-3p	5-3p	
5-1d	5-3d		3-3s	3-3p	CMFGEN	4-3p	5-3d	
5-1d	5-3f		3-3s	3-3d	CMFGEN	4-3p	5-3f	
			3-3s	4-3s	CMFGEN			
5-1f	2-3s		3-3s	4-3p	CMFGEN	4-3d	4-3f	CMFGEN
5-1f	2-3p		3-3s	4-3d	CMFGEN	4-3d	5-3s	
5-1f	3-3s		3-3s	4-3f	CMFGEN	4-3d	5-3p	
5-1f	3-3p		3-3s	5-3s		4-3d	5-3d	
5-1f	3-3d		3-3s	5-3p		4-3d	5-3f	
5-1f	4-3s		3-3s	5-3d				
5-1f	4-3p		3-3s	5-3f		4-3f	5-3s	
5-1f	4-3d					4-3f	5-3p	
5-1f	4-3f		3-3p	3-3d	CMFGEN	4-3f	5-3d	
5-1f	5-3s		3-3p	4-3s	CMFGEN	4-3f	5-3f	
5-1f	5-3p		3-3p	4-3p	CMFGEN			
5-1f	5-3d		3-3p	4-3d	CMFGEN	5-3s	5-3p	
5-1f	5-3f		3-3p	4-3f	CMFGEN	5-3s	5-3d	
			3-3p	5-3s		5-3s	5-3f	
2-3s	2-3p	CMFGEN	3-3p	5-3p				
2-3s	3-3s	CMFGEN	3-3p	5-3d		5-3p	5-3d	
2-3s	3-3p	CMFGEN	3-3p	5-3f		5-3p	5-3f	
2-3s	3-3d	CMFGEN				5-3d	5-3f	
2-3s	4-3s	CMFGEN	3-3d	4-3s	CMFGEN			
2-3s	4-3p	CMFGEN	3-3d	4-3p	CMFGEN			

APPENDIX C

HYDROGEN LEVEL DESIGNATIONS

Level	Our Number	Chianti	CMFGEN	Level	Our Number	Chianti	CMFGEN
1 S	1	1	1	n = 10	20	----	16
2 S	2	2	2	n = 11	21	----	17
2 P	3	3, 4	3	n = 12	22	----	18
3 S	4	5	4	n = 13	23	----	19
3 P	5	6, 7	5	n = 14	24	----	20
3 D	6	8, 9	6	n = 15	25	----	21
4 S	7	10	7	n = 16	26	----	22
4 P	8	11, 12	8	n = 17	27	----	23
4 D	9	13, 14	9	n = 18	28	----	24
4 F	10	15, 16	10	n = 19	29	----	25
5 S	11	17	----	n = 20	30	----	26
5 P	12	18, 19	18				
5 D	13	20, 21	19				
5 F	14	22, 23	20				
5 G	15	24, 25	----				
n = 5	----	----	11				
n = 6	16	----	12				
n = 7	17	----	13				
n = 8	18	----	14				
n = 9	19	----	15				

APPENDIX D

HELIUM LEVEL DESIGNATIONS

Level	Our Number	Chianti	CMFGEN	Level	Our Number	Chianti	CMFGEN
$1\ ^1S$	1	1	1	$4\ ^3P$	21	20,21,22	14
$2\ ^1S$	2	3	3	$4\ ^3D$	22	23,24,24	15
$2\ ^1P$	3	7	5	$4\ ^3F$	23	27,28,29	17
$3\ ^1S$	4	9	7	$5\ ^3S$	24	32	----
$3\ ^1P$	5	----	11	$5\ ^3P$	25	34,35,36	----
$3\ ^1D$	6	16	10	$5\ ^3D$	26	37,38,39	----
$4\ ^1S$	7	19	13	$5\ ^3F$	27	41,42,43	----
$4\ ^1P$	8	----	19				
$4\ ^1D$	9	26	16				
$4\ ^1F$	10	30	18				
$5\ ^1S$	11	33	----				
$5\ ^1P$	12	----	----				
$5\ ^1D$	13	40	----				
$5\ ^1F$	14	44	----				
$2\ ^3S$	15	2	2				
$2\ ^3P$	16	4,5,6	4				
$3\ ^3S$	17	8	6				
$3\ ^3P$	18	10,11,12	8				
$3\ ^3D$	19	13,14,15	9				
$4\ ^3S$	20	18	12				

APPENDIX E

SUBROUTINES IN THE RADIATIVE TRANSFER PROGRAM

INIT	Initialize the program.
REDHYD	Reads hydrogen level population.
REDHEL	Reads helium level population.
REDBIGVJ	Reads mean intensity.
SETSOU	Set the source function below the He 1 Ionization.
STSOU2	Set the source function beyond the He 1 Ionization.
MODEL	Calculate the Radiative transfer at each point below He 1 Ionization.
MODEL2	Calculate the Radiative transfer at each point above He 1 Ionization.
FINDJ	Calculate the mean intensity at a point in the atmosphere.
PHCONT	Calculate photoionization rates from each level of hydrogen.
HECONT	Calculate photoionization rates from each level of helium.
OTHERS	Set the escape probability for hydrogen.
HEOTHR	Set the escape probability for helium.
RATES	Calculate the transition rates for hydrogen.
HERATE	Calculate transition rates for helium.
NEWPOP	Set the new level population for hydrogen.
HELPOP	Set the new level population for helium.
GAUSS	Solve N simultaneous equations by using Gaussian elimination.
WRTHYD	Write out hydrogen level population into direct access file.
WRTHEL	Write out helium level population into direct access file.

REFERENCES

Abbet, W.P., and Hawley, S.L. 1999, *Astophysical Journal*, 521, 906-919.

Abramowitz, M., and Stegun, I.A., 1970, "Handbook of Mathematical Functions", Dover, New York.

Adam, J., Storzer, H., Shaviv, G., and Wehrse, R. 1988, *Astronomy and Astrophysics*, 193, L1-L3.

Allred, J.C., Hawley, S.L., Abbett, W.P., and Carlsson, M. 2005, *Astrophysical Journal*, 630, 573-586.

Annamaneni, P. 2002, an Introduction to Radiative Transfer, Cambridge University Press.

Balbus, S.A., Hawley, J.F. 1991, *Astrophysical Journal*, 376, 214-222.

Berrington, K.A., and Kingston, A.E. 1987, *J. Phys. B: At. Mol. Phys.*, 20, 6631.

Brocklehurst, M. 1971, *M.N.R.A.S.*, 153, 471-490.

Burgess, A. 1964, Mem. R.A.S., 69, 1.

Cannizzo, J.K., Shafter, A.W., and Wheeler, J.C. 1988, *Astrophysical Journal*, 333, 227-235.

Cannizzo, J.K. 1993, *Astrophysical Journal*, 419, 318-336.

Capriotti, E.R. 1964, *Astrophysical Journal*, 139, 225.

Carlsson, M., and Stein, R.F. 1997, *Astrophysical Journal*, 481, 500.

Donati-Falchi, A., Falciani, R., and Smaldone, L.A., 1984a, Astron. & Astrophys., **131**, 256.

Donati-Falchi, A., Falciani, R., Sambuco, A.M., Smaldone, L.A., 1984b, Astron. & Astrophys. Supp. Ser., **55**, 425.

Feautrier, P., 1964, *C.R. Acad. Sci. Paris*, **258**, 3189.

Gingold, R.A., and Monaghan, J.J. 1977, *Royal Astronomical Society, Monthly Notices*, 181, 375-389.

Green, L.C., Rush, P.P., and Chandler, C.D. 1957, *Astrophysical Journal*, 3, 37.

Hillier, D.J., and Lanz, T. 2001, *ASP Conference Series*, 247, 343-350.

Howland, K., 1995, "Absolute Visual Magnitudes and Emission Line Strengths from Accretion Disks of Cataclysmic Variable Stars", Master's Thesis, Central Michigan University.

Hughes, D., Paczuski, R.O., Dendy, P., and McClements, K.G. 2003, *Physical Review Letters*, 90, 13.

Johnson, L.C. 1972, *Astrophysical Journal*, 174, 227-236.

Lucy, L.B. 1977, *Astronomical Journal*, 82(12), 1013-1024.

Meyer, F., and Meyer-Hofmeister, E. 1981, *Astronomy and Astrophysics*, 104, L10-L12.

Meyer, F., and Meyer-Hofmeister, E. 1982, *Astronomy and Astrophysics*, 106, 34-42.

Meyer, F., and Meyer-Hofmeister, E. 1983, *Astronomy and Astrophysics*, 128, 420-425.

Mihalas, D. 1978, *Stellar Atmospheres* (San Francisco: Freeman).

Monaghan, J.J. 1992, *Annual Review Astronomy and Astrophysics*, 30, 543-574.

Neidig, D.F., and Wiborg, P.H., 1984, Solar Physics, **92**, 217.

Nguyen, T.Q. 1993, "Non-LTE Calculation of Helium I Line Emission from Cataclysmic Variable Stars", Master's thesis, Central Michigan University.

Osterbrock, D.E., and Ferland, G.J. 2006, Astrophysics of Gaseous Nebulae and Active Galactic Nuclei, University Science Books.

Park, J. 2010, "Modeling Flares on the Accretion Disk", Master's Thesis, Central Michigan University.

Romanova, M.M., Ustyugova, G.V., Koldoba, A.V., Chechetkin, A.V., and Lovelace, R.V.E. 1998, *Astrophysical Journal*, 500, 703-713.

Rose, S.J. 1998, *J. Phys. B: At. Mol. Opt. Phys*, 31, 2129-2144.

Seaton, M.J. 1959, *M.N.R.A.S., 119, 81.*

Shakura, N.I., and Sunyaev, R.A. 1973, *Astronomy and Astrophysics*, 24, 337-355.

Tandberg-Hanssen, E., and Emslie, A.G. 1988, *The Physics of Solar Flares. Cambridge:* Cambridge University Press.

Theodosiou, C.E. 1987, Atomic Data and Nuclear Data Tables, 36, 97.

Tout, C.A., and Pringle, J.E. 1992, *Mon. Not. R. Astron. Soc.*, 259, 604-612.

Tylenda, R. 1980, *Acta Astronomica*, 30(4), 433-448.

Tylenda, R. 1981a, *Acta Astronomica*, 31, 127.

Tylenda, R. 1981b, *Acta Astronomica*, 31, 267.

Vriens, L., and Smeets, A.H.M. 1980, *Phys, Rev. A*, 22, 940.

Warner, B. 1995, Cataclysmic Variable *Stars*, Cambridge University Press.

Wiese, W.L., Smith, M.W., and Glennon, B.M. 1966, Atomic Transition Probabilities, 1, 153p, NSRDS-NBS 4.

Williams, G., and Maletesta, K. 2001, *Astronomical Journal*, 123, 1095-1105.

Williams, G.A., 1983, *The Astrophysical Journal Supplement Series*, 53, 523-551.

Williams, G.A., and Shipman, H.L. 1988, *Astrophysical Journal*, 326, 738-750.

Williams, G.A. 1992, *In ASP Conf. Ser. 29, Vina Del Mar Workshop on Cataclysmic Variable Stars, ASP Conference Series*, 29, 90-98.

Williams, R.E. 1980, *Astrophysical Journal*, 235, 939-944.

Williams, R.E., and Ferguson, D.F. 1982, *Astrophysical Journal*, 257, 672-685.